Chapter 1
Hard X-ray Photoemission: An Overview and Future Perspective

Charles S. Fadley

Abstract The various aspects of hard X-ray photoemission are reviewed, including in particular more newly developed directions of measurement, but also with references to other chapters in this book or prior publications in which additional details can be found. An overview of the different dimensions of the technique, including a look at promising future directions, is presented.

1.1 Introduction

Although hard X-ray photoemission (HXPS, HAXPES, HX-PES,…) in fact has a long history, as reviewed elsewhere in this book by Svensson, Sokolowski, and Martensson, by Pianetta and Lindau, who pioneered it with synchrotron radiation (SR) excitation at SSRL [1], and by Kobayashi, who discusses the first undulator-based activities at SPring-8, it is really only in the last 15 years or so that the development of beamlines, spectrometers, and even laboratory sources, has led to its rapid growth. By now, various statistics indicate the rapid growth of the technique. The number of papers appearing and the citations to them are growing exponentially, as shown from the Web of Science statistics in Fig. 1.1, which certainly represent conservative numbers due to the fact that authors may not always use our search keywords in publications, and in fact probably do this less with time as the technique becomes more commonly used. Some overall numbers

C.S. Fadley (✉)
Department of Physics, University of California Davis, Davis, CA 95616, USA
e-mail: fadley@physics.ucdavis.edu

C.S. Fadley
Materials Sciences Division, Lawrence Berkeley National Laboratory, Berkeley CA 94720, USA

J.C. Woicik (ed.), *Hard X-ray Photoelectron Spectroscopy (HAXPES)*,
Springer Series in Surface Sciences 59, DOI 10.1007/978-3-319-24043-5_1

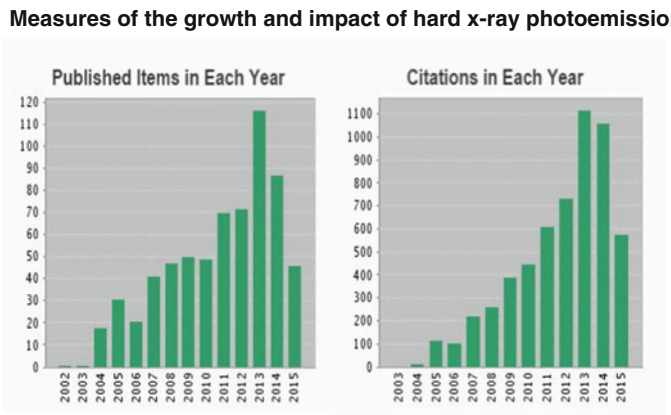

Fig. 1.1 A Web of Science plot of the number of publications and citations versus time involving the keywords "hard X-ray photoelectron spectroscopy" or "hard X-ray photoemission" or "high energy photoelectron spectroscopy" or "high kinetic energy photoelectron diffraction" or "hard X-ray photoelectron microscopy" or "HXPS" or "HAXPES" or "HX-PES" or "HAXPEEM". This data is from June, 2015

from this search in June, 2015 are about 640 publications, 1000 citations per year, 5600 citations in total, 9 cites/paper, and an h-index of 38. These publications have furthermore appeared in leading high-impact journals. There are also currently approximately 20 synchrotron radiation beamlines running or in construction/commissioning that are at least partly dedicated to HXPS, in alphabetical order at: ALS, BESSY II, CLS, Diamond, Petra III, NSRRC, NSLS-2, Soleil, and SPring-8, with by far the largest number at SPring-8, still the leading facility in this technique. Commercial systems permitting in-laboratory monochromatized HXPS are also now available. Finally, there has been a continuing series of international workshops and by now international conferences on HXPS, with programs and proceedings often online [2–10].

Beyond this, and more importantly, the technique has by now been applied to the full range of forefront materials issues in physics and chemistry, including bulk, surface, and buried interface studies, as beautifully demonstrated in various chapters in this book, e.g., by Browning—photoelectron microscopy of various materials types; Chambers-oxide heterostructures; Gray—dilute magnetic semiconductors; Kobayashi—a broad range of advanced materials and device structures; Liu and Bluhm—ambient pressure photoemission studies of surfaces and interfaces, including very recent use of hard X-ray excitation [11]; Taguchi and Panaccionne, plus Tjeng et al.—strongly correlated materials; Mukherjee, Santra and Sarma—nanostructures; Weiland, Rumaiz, and Woicik, plus Lysaght and Woicik—band alignments and semiconductors, and Zegenhagen, Lee, and Thiess—oxides and superconductors. In addition, it is clear that HXPS can be very fruitfully applied in atomic and molecular physics, as overviewed by Simon, Piancastelli, and Lindle. I here also note with deep sadness our loss last year of Dennis Lindle, a true pioneer

in applying hard X-ray excitation to atomic and molecular physics with his work at the Advanced Light Source.

I will not attempt here to repeat what is already so well reviewed and presented in the above-cited chapters devoted to applications of HXPS, but will limit this overview to discussing the basic principles of the technique, including its strengths, weaknesses, some new directions, and challenges for future experimental and theoretical developments. This discussion will thus more directly relate to other chapters on the fundamental physics of photoemission in the hard X-ray regime by Braun, Ebert, and Minar—photoemission theory; Browning-photoelectron microscopy; Grosvenor et al.—final-state effects; Kayanuma-recoil effects; Powell and Tanuma—inelastic mean free paths; and Rossnagel et al.—time-resolved measurements. Some additional new measurement methods will be pointed out, for example, involving standing-wave (SW) or near-total-reflection (NTR) excitation from multilayer heterostructures, which are not covered elsewhere in this book.

Finally, the reader is directed to several other overviews and special journal issues involving HXPS and its relationship to conventional XPS at less than 2 keV that have been published [12–14], including some from my group [15–20], and to which specific references will subsequently be made.

In concluding this introduction, it is worth noting the various measuring modalities in photoemission in general, which are illustrated in Fig. 1.2, all of which will be discussed individually in the following sections.

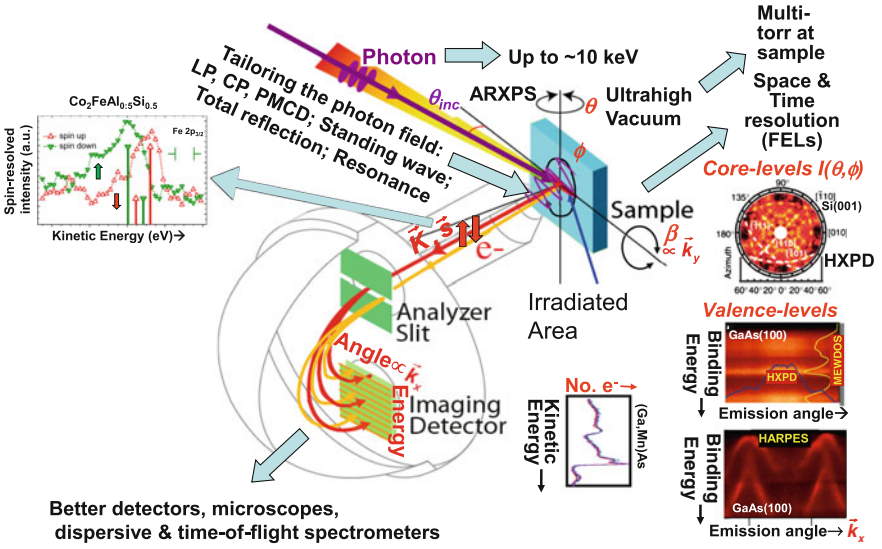

Fig. 1.2 Schematic illustration of the different measurement modalities in photoemission, with *inset* examples discussed later in this and other chapters of this book. The core schematic from which this figure is derived is from Y. Takata

1.2 Basic Effects and Considerations—Advantages, Disadvantages, and Challenges

1.2.1 Probing Depth

Of course, the ability to probe more deeply into a sample and reduce the importance of surface effects is a primary reason for using hard X-ray excitation in photoemission. Hard X-ray is here defined as >2 keV, since that is typically the energy above which crystal monochromators, instead of grating monochromators, must be used. Some prefer to call the range of ca. 2–10 keV that is most commonly used in HXPS measurements "tender" X-rays.

The probing depth is controlled by the inelastic mean free path (IMFP), and Fig. 1.3 shows a compilation of values for 41 elements calculated from optical data and leading to the much-used TPP-2 M formula for estimating them, from the work of Tanuma et al. [21]. This method and its application to HXPS are discussed in more detail in the chapter by Tanuma and Powell.

The conclusions from this and other recent experimental work [22, 23] are that the only reliable way to increase bulk or buried layer and interface sensitivity for all material types is to go to higher photon energies in the soft X-ray (ca. 0.5–2 keV) or hard X-ray (ca. 2–10 keV) regime. Going to very low photon energies with laser excitation is also often discussed as a method for enhancing bulk sensitivity [24], but it seems clear that this will not be a universal benefit for all materials, and may only be true for those with a significant bandgap. Further experimental and theoretical study of this last point is needed.

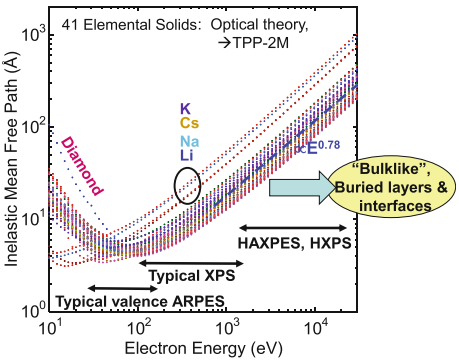

Fig. 1.3 Energy dependence of electron inelastic mean free paths as calculated from optical properties for 41 elements, with values closely related to the TTP-2M formula (From [21])

1.2.2 Ease of Spectral Analysis

There are several ways in which spectral analysis is simpler at higher photon energies:

- The inelastic backgrounds under spectra are significantly reduced, thus making the allowance for them in fitting to derive various peak intensities easier.
- Auger spectra are in general further apart, thus creating less overlap with photoelectron peaks whose detailed analysis is desired.
- Peak intensity analyses:
  The analysis of peak intensities via standard formulas for core photoelectron emission, such as that shown in (1.1) and Fig. 1.4 for a typical $n\ell j$ level in atom Q, with an incident flux of $I_{hv}(x, y, z, \hat{\varepsilon})$, radiation polarization of $\hat{\varepsilon}$, an IMFP of $\Lambda_e(E_{kin})$, and a spectrometer acceptance solid angle over the surface of $\Omega(E_{kin}, x, y)$,

$$I(Qn\ell j) = C \int_0^\infty I_{hv}(x, y, z, \hat{\varepsilon}) \rho_Q(x, y, z) \frac{d\sigma_{Qn\ell j}(hv, \hat{\varepsilon})}{d\Omega} \times \exp\left[-\frac{z}{\Lambda_e(E_{kin}) \sin\theta}\right] \Omega(E_{kin}, x, y) dx dy dz \tag{1.1}$$

  and as used e.g. in angle-resolved XPS (ARXPS) depth profile analyses, are simpler because:

  – The IMFPs $\Lambda_e(E_{kin})$ of different peaks, although kinetic energy dependent, can have much less variation than with lower energy excitation, because the higher kinetic energies of less-bound electronic levels are closer in relative values.
  – The instrument response function, indicated as the solid-angle of acceptance $\Omega(E_{kin}, x, y)$ in Fig. 1.4, will also tend to be more nearly constant over a set of peaks with high, and thus very nearly equal, kinetic energies.
  – The effects of elastic scattering in smearing out the photoelectron intensity distribution, indicated by the scattering factor $f(\theta_{scatt})$ in Fig. 1.4, will be less pronounced, due to the generally increasing forward focusing effect as energy is increased.
  – The effect of refraction in crossing the inner potential barrier V_0 will be less as energy is increased.
  – The effects of surface-associated inelastic scattering will also be reduced as the kinetic energy increases [25].
  – In valence photoemission, it is also well known [26, 27] that the photoelectric cross section becomes more and more dominated by the core region of each atom as energy is increased, thus permitting an approximate decomposition of a valence spectrum in the high-energy XPS or density-of-states (DOS) limit into a sum of partial intensities based on orbital-projected DOSs and atomic differential cross sections, as indicated in (1.2) below:

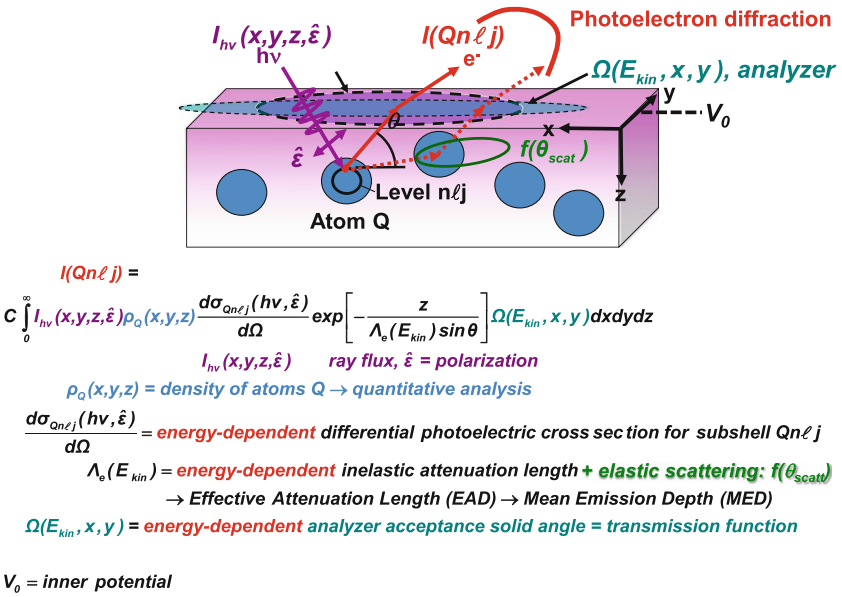

Fig. 1.4 Core photoelectron emission, with a general sample and experimental configuration indicated, along with the standard formula for analyzing intensities, also appearing in (1.1)

$$
\begin{aligned}
I_{total}(E_{kin}) &= \sum_{Qn\ell j} I(E_{kin}, Qn\ell j) \\
&= \sum_{Qn\ell j} C' \int_0^\infty I_{hv}(x,y,z,\hat{\varepsilon})\rho_{Qn\ell j}(E_b,x,y,z)\frac{d\sigma_{Qn\ell j}(hv,\hat{\varepsilon})}{d\Omega} \\
&\quad \times \exp\left[-\frac{z}{\Lambda_e(E_{kin})\sin\theta}\right]\Omega(E_{kin},x,y)dxdydz
\end{aligned}
\tag{1.2}
$$

with $\rho_{Qn\ell j}(E_b,x,y,z)$ the projected density of states for the $Qn\ell j$ orbital at a given binding energy and position in the sample.

Thus, the simple formulas shown in (1.1) or in (1.2) will be more quantitative for HXPS in many situations, permitting simpler spectral analyses of both core and valence spectra.

It is important finally to note that a user-friendly program exists for calculating spectra for core-level emission, namely Simulation of Electron Spectra for Surface Analysis (SESSA), whose input databases have recently been extended to cover hard X-ray excitation [28, 29]. This program includes all of the physical effects indicated in Fig. 1.4, with elastic scattering assumed to be from an array of randomly positioned atoms, although it does not include refraction effects in crossing the inner potential.

1.2.3 Photoelectric Cross Sections, Including Polarization Effects

Beyond these considerations however, is the clear challenge that photoelectric cross sections decrease dramatically as photon energy, or equivalenty kinetic energy E_{kin} is increased [30–32], varying in a high-energy asymptotic limit roughly as $\sigma_{Qn\ell j}(E_{kin}) \propto (E_{kin})^{-7/2} = (E_{kin})^{-3.5}$ for s subshells and $\propto (E_{kin})^{-9/2} = (E_{kin})^{-4.5}$ for p, d, and f subshells, but with more accurate calculations for specific cases in the two references mentioned. Figure 1.5 illustrates this decrease with calculated cross sections [30] for the subshells of Mn and O over 1–10 keV spanning the most common HXPS range. Thus, the development of HXPS has required the design of beamlines, including enhanced intensity with undulator excitation [33], and laboratory sources with the highest possible intensities, as well as spectrometers with the highest solid angles of acceptance, with the latter for example now going up to ±30° in commercial hemispherical electrostatic instruments and up to ±45° in custom-designed systems [34]. The possibility of time-of-flight analysis to further increase intensities is also being discussed [35, 36]. However, with present SR HXPS facilities, it is still possible to saturate any existing detector for intense core levels, and research and development thus needs to be done for higher-throughput electron detectors capable of the GHz-regime [37], as compared to the current ∼1 MHz for 2D detection, and ∼10 MHz for 1D detection.

Another important consequence of this energy variation for valence-level studies is that subshells with lower ℓ for a given n that thus exhibit more oscillations in the core region decay in intensity less rapidly than those with higher ℓ. Figure 1.5 illustrates that, for example, Mn 3s decays less rapidly than Mn 3p, and Mn 3p less

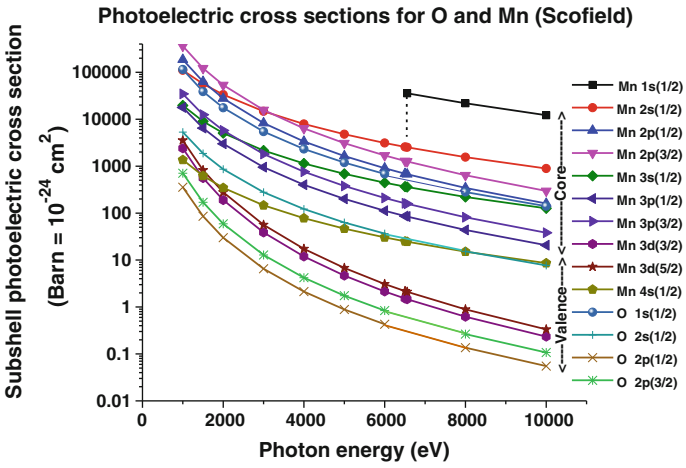

Fig. 1.5 Relativistic subshell cross sections for Mn and O as a function of photon energy over the region 1–10 keV (From [30])

rapidly than Mn 3d. A similar thing is found for O 2s, which decays less rapidly than O 2p. These variations already make the asymptotic formulas above, which do not discriminate p, d, and f cross sections, look inaccurate for typical HXPS energies. In fact, the exponents derived with cross section ratios from Fig. 1.5 at 8 and 10 keV, by assuming that (Cross section at hν = 10,000)/(Cross section at hν = 8000) = (E_{kin} at 10,000 eV)^m/(E_{kin} at 8000 eV)^m yield values of m = −2.4 to −2.6 for Mn 1s, Mn 2s, Mn 3s, and Mn 4s, or about 5/2, with O 1s and O 2s being somewhat higher at m = 3.0, or about 6/2. Mn 2p and Mn 3p show m = −3.3 to −3.4, and O 2p larger values of m = −3.9 to −4.0, or about 7/2–8/2. Lastly, Mn 3d has the largest value at m = −4.2 to −4.3, approaching the asymptotic limit of 9/2. Thus, these values only roughly agree with, and span a greater range than, the asymptotic numbers above, and of course clearly show the trends with ℓ for a given n already mentioned.

Other more complex but important variations in relative intensity also occur if one considers the important case of valence-electron spectra. For example, by 10 keV the valence spectrum of a sample with both Mn and O in it (as would be typical for a transition metal (TM) oxide) is expected to be dominated by O 2p and Mn 4s character.

Another cross-section effect that must be allowed for as energy increases is the increasing importance of non-dipole terms [31, 32, 38] (see also chapter by Simon, Piancastelli, and Lindle). These can be broken into two types, depending on whether core-like intensities are involved or momentum-resolved angle-resolved photoemission (ARPES) valence intensities are being analyzed. In the first case, standard correction parameters to the usual dipole formula are available for a number of atoms and energies [31, 32, 38], and these can be interpolated and extrapolated for a given case at hand. For ARPES, or more appropriately, soft- and hard-X-ray ARPES (SARPES and HARPES, respectively), a correction due to the photon momentum is needed in the momentum-conservation equation, as discussed elsewhere [15, 18, 19, 39, 40], later in this chapter, and in the chapter by Gray in this book. This is a simple correction to do as well, provided that the experimental geometry is precisely defined.

As another more recently realized aspect of hard X-ray photoelectric cross sections, it has recently been shown by Drube et al. that interchannel coupling effects that are essentially resonant photoemission with deep core levels can significantly influence the relative intensities of shallower core levels. For example, the Ag $3d_{3/2,5/2}$ intensities at binding energies of ∼374 and 368 eV are influenced by as much as 30 % in scanning the photon energy over the Ag $2p_{1/2,3/2}$ resonances at ∼3560 and 3250 eV. Thus, it may be necessary to avoid such resonances by as much as a few hundred eV if a simple quantitative analysis according to equations such as those in (1.1) or (1.2) is to be valid.

As more and more hard X-ray beamlines are permitting the variation of polarization through the use of diamond phase retarders [41, 42], it is important to note the strong effects that this can have on the differential photoelectric cross sections. This is particularly important for valence-level spectra in which the different orbital contributions can be resolved in energy through the projected densities of states, as

indicated in (1.2). As a simple illustration of this, Figs. 1.6 and 1.7 show some calculated differential cross sections for the Cu $3d_{z2}$ and O $2p_z$ orbitals, at two energies of 0.8 and 5 keV and three different polarization orientations along x, y, and z. These have been calculated in a non-relativistic limit using equations published some time ago [43], with extrapolations of radial matrix elements and phase shifts for the $\ell \pm 1$ interfering channels to 5 keV using the data in [43], and an online program due to Nemšák et al. that permits calculating them for an arbitrary experimental geometry [44]. Of course, for any s subshell in the dipole limit, the cross section looks like a p wave oriented along the polarization direction, that is of the functional form given at the left of Fig. 1.7, since there is only one channel in the final state, and so will have a node for emission perpendicular to the polarization vector for all three orientations in this figure.

From these calculations for more complex non-s subshells, it is clear that varying polarization away from the special case of being parallel to the electron emission

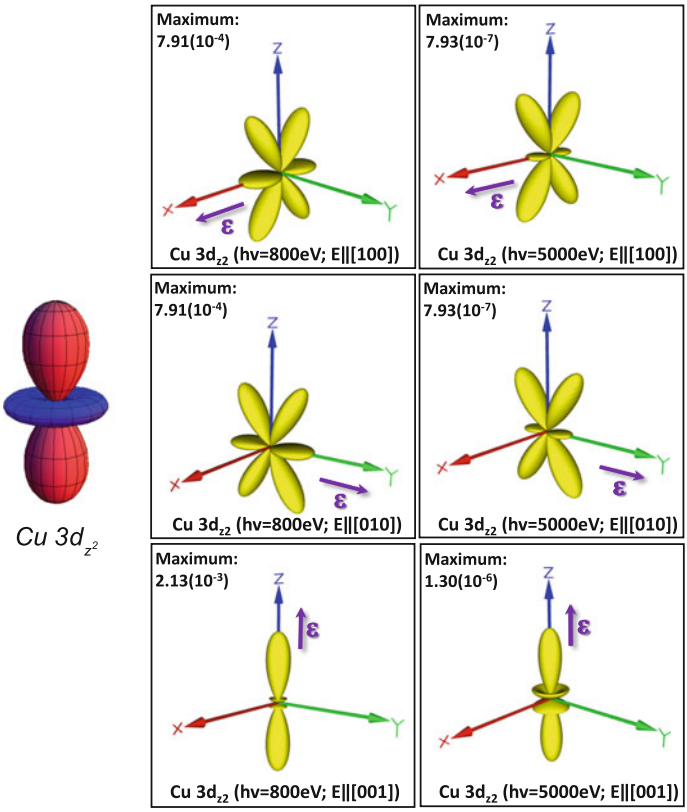

Fig. 1.6 Non-relativistic dipole-approximation cross sections for the Cu $3d_{z2}$ orbital, for three different polarization directions and at 800 and 5000 eV photon energies. The maximum value of each contour is indicated in the *inset* (From [44])

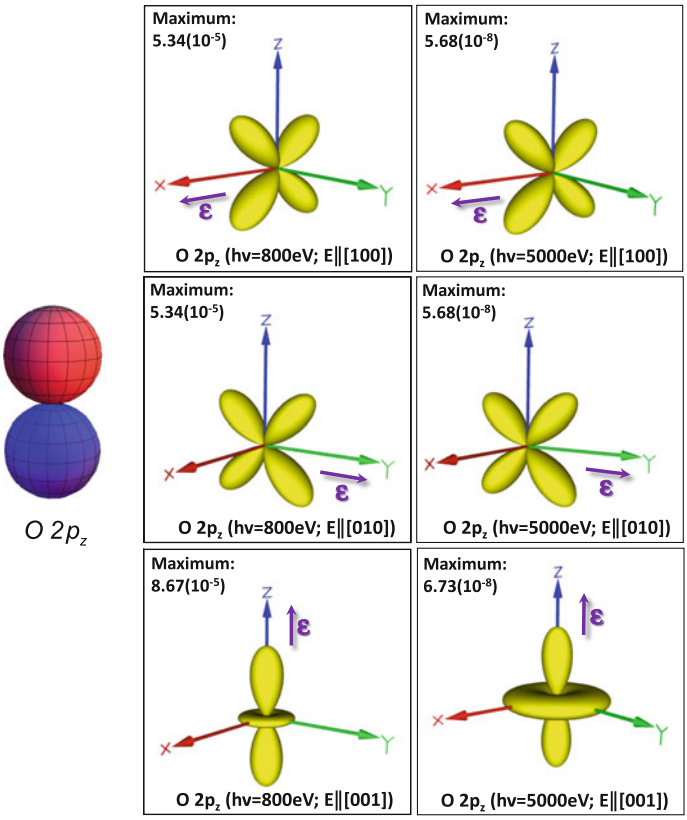

Fig. 1.7 As Fig. 1.6, but for the O $2p_z$ cross sections (From [44])

direction (a special case which is known to yield cross sections of exactly the same form as the orbital shape angular shape [43]), can yield dramatic changes. For example, the Cu $3d_{z2}$ cross section tends to look somewhat like the orbital for z polarization, but is completely different in x and y polarization. There are also some significant changes as the energy is increased from 800 to 5000, particularly for x and y polarization. Similar things are true for the O $2p_z$ cross section, again tending to look like the orbital for z polarization, but changing dramatically so as to have nodes along the orbital direction with x and y polarization. Although more accurate relativistic calculations allowing for non-dipole effects would no doubt be somewhat different from these results, the changes with polarization and energy in Figs. 1.6 and 1.7 would be expected to be semi-quantitatively maintained.

As one simple illustration of the utility of polarization in valence-band studies, it is pointed out in in recent publications [42, 45], and in the chapter by Tjeng et al., that it can be useful to emit electrons perpendicular to the polarization direction in order to suppress the strong TM 4s contributions in TM oxide valence spectra, so as to more directly see the transition metal 3d contributions (cf. Fig. 1.5). Figures 1.6

and 1.7 make it clear that other polarization-emission geometries could be useful in enhancing or de-enhancing the contributions of different orbitals. Making use of such variations in cross sections with polarization is of course also a type of linear dichroism, and will be a very useful technique in future HXPS studies.

Finally, it is important to note that elastic scattering, as indicated schematically in Fig. 1.4, will minimally tend to smear out the various features seen in purely atomic cross sections such as those in Figs. 1.6 and 1.7, but also for any atomically ordered system to produce strong modulations due to photoelectron diffraction, as discussed further below.

1.2.4 Chemical Shifts, Multiplet Splittings, and Satellites in Core-Level Spectra

It is obvious that core-spectra in HXPS can be mined for the same kinds of information as in soft X-ray excited spectra: chemical state from chemical shifts, orbital occupations and spin from multiplet structure, and local bonding information from satellites, whether they are described as shake-up or final-state screening in nature. But it was realized early on by Horiba et al. in work on a colossal magnetoresistive manganite [46], subsequently in work on high temperature superconductors [47] and later on dilute magnetic semiconductors (DMSs) [48] that going to higher energies permits observing extremely sharp low-binding-energy satellites on transition-metal 2p spectra, and that these can be interpreted in terms of bulk screening by highly delocalized valence electrons near the Fermi level [49]. An example of this kind of data for the DMS $Ga_{0.97}Mn_{0.03}As$ is shown in Fig. 1.8, for which the Mn $2p_{3/2}$ peak shows a very strong screening satellite of this type. These final-state effects provide yet another handle on valence electronic structure and have been found to be sensitive for example to the presence of ferromagnetic order [46, 48]. The spectrum in Fig. 1.8 also exhibits a multiplet splitting for the Mn 3s spectrum that can be used to estimate the spin on this atom. These final state effects and their interpretation are reviewed in the chapter by Grosvenor et al. and also discussed in the chapter by Taguchi and Panaccione.

1.2.5 Recoil Effects

Recoil effects in HXPS were first explored by Takata et al. [50], and are discussed in detail in the chapter by Kayanuma. They have been found to affect both core level- and valence level-spectra [50–52], and must be considered as sources of both peak shifts to effectively higher binding energies, and peak broadening. Figure 1.9b provides a simple way to estimate the maximum magnitude of the peak shift, in the simplest assumption that it is a single-atom phenomenon. However, it is also clear

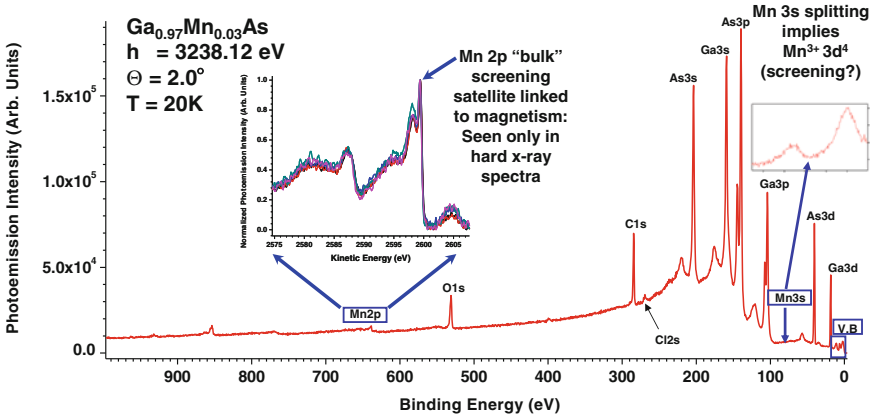

Fig. 1.8 Survey spectrum from the dilute magnetic semiconductor $Ga_{0.97}Mn_{0.03}As(001)$ with 3.2 keV excitation, and with *enlarged insets* from scanning longer on Mn 2p and 3s. Mn 2p reveals a sharp final-state screening peak only seen with hard X-ray excitation. Mn 3s show a doublet due to multiplet splitting that can be used to estimate the spin of Mn. Data from SPring-8 (From [40])

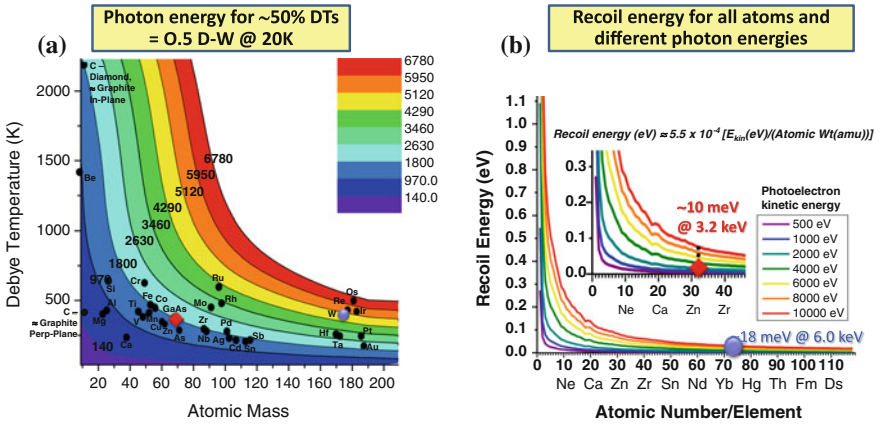

Fig. 1.9 Calculated parameters for estimating the feasibility of ARPES at higher energies, including (**a**) contours for various photon energies to yield a photoemission Debye-Waller factor W(T) of 0.5 at 20 K, and **b** the recoil energy for all atoms as a function of photon energy. Values for two first demonstration cases W and GaAs studied with hard X-rays [39] are highlighted (From [55])

from work to date that it is the detailed vibrational coupling of a given atom to its near neighbors that controls the magnitude of the recoil shift [52], suggesting what has been called "recoil spectroscopy" as a local probe of such local bonding effects, including those in valence spectra [53].

A particularly illuminating recent example of the observation of recoil effects in gas-phase HXPS is for Ne 1s emission [54], for which the p-wave nature of the

cross section means that the emission of the photoelectrons is strongly biased toward being either parallel or anti-parallel to the polarization vector, as shown in Fig. 1.10a. But if the photoelectrons and the subsequent KLL Auger electrons are detected along the polarization as shown, then the Auger electrons will be Doppler shifted in energy depending on the direction of emission of the photoelectrons. The turning on of this effect is seen as photon energy is increased into the 10 keV regime in Fig. 1.10b. Such effects are presumably also present in solids as well, and will be a source of broadening in Auger peak widths at higher energies. This and other aspects of HXPS in atomic and molecular physics are discussed in the chapter by Simon, Piancastelli, and Lindle.

As a final comment on recoil, the use of a Debye-Waller (D-W) factor to estimate the recoil-free fraction for a given excitation is directly related to the analysis of Mössbauer spectra [50], and also to the degree to which HXPS valence spectra can be expected to exhibit momentum-resolved electronic structure via direct transitions in angle-resolved photoemission (ARPES) [55]. Figure 1.9a in fact permits estimating the fraction of momentum-resolved transitions as a function of Debye temperature, atomic mass, and photon energy. When the D-W factor is very small, one speaks of being in the XPS limit or more precisely the matrix-element-weighted density of states (MEWDOS) limit. This continuum between the ARPES limit at low temperature and/or low energy and the XPS limit at high temperature and/or high energy is discussed further below, in prior publications [18, 39, 40, 55], and in the chapter by Gray.

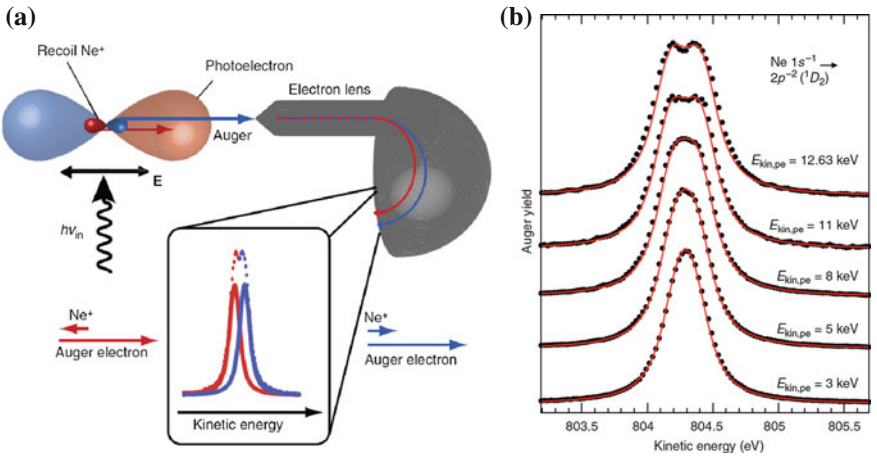

Fig. 1.10 Doppler effect on Auger emission from a free atom. **a** The two basic recoil directions of Ne 1s emission relative to the polarization directions of the incident X-ray, depending on whether the photoelectron is emitted toward the spectrometer or away from it. The expectation for this effect on a subsequent Auger emission spectrum is indicated in the *inset*. **b** Actual Auger spectra for the transition Ne^{+1} $1s^{-1} \rightarrow Ne^{+2}$ $2p^{-2}$ ($^1D_2$) + Auger electron, as photon energy is increased. Data from Soleil (From [54])

1.2.6 Circular and Linear Dichroism

Making use of linear polarization to accentuate different orbital contributions has been discussed above under cross sections, but beyond this is the well-known magnetic circular dichroism (MCD) in magnetic systems, first observed in soft X-ray photoemission from Fe by Schneider et al. [56], and first observed in HXPS from Fe_3O_4 and Zn-doped Fe_3O_4 by Ueda et al. [57]. To distinguish photoemission MCD from the more commonly practiced X-ray absorption MCD (XMCD), it seems worthwhile to designate the photoemission variant as PMCD. Although the much-used sum rules of XMCD have no simple analogues in PMCD, PMCD data nonetheless permits assessing magnetic order, including at buried interfaces. Linear magnetic dichroism in photoemission (PMLD) has also been measured, and often is referred to with the suffix AD to denote that it is measured in angular distributions. Note to Editor: There are terms in the figure caption that I noticed are not defined in the text. Some PMCD results from the first HXPS study are presented in Fig. 1.11 [57], and in Fig. 1.12c–e from a more recent study of a buried layer of $Co_2FeAl_{0:5}Si_{0.5}$ [58].

PMCD has in fact been used in connection with soft X-ray standing-wave excitation (to be introduced below) to probe the depth distribution of magnetic order through buried interfaces of Fe/Cr [59] and Fe/MgO [60], and such measurements should be possible with hard X-ray excitation.

1.2.7 Spin-Resolved Spectra

Adding the spin dimension to HXPS is an obvious next step that would increase the ability to probe magnetic systems enormously, and first measurements of spin-resolved spectra have already been made on the same buried layer containing Fe [58], as shown in Fig. 1.12a–c.

Novel imaging spin detectors [61, 62] and other more efficient spin detectors that should be suitable for HXPS [63] are also being developed that promise a factor of $\sim$100, if not more, in speed, and some of these are being implemented for HXPS

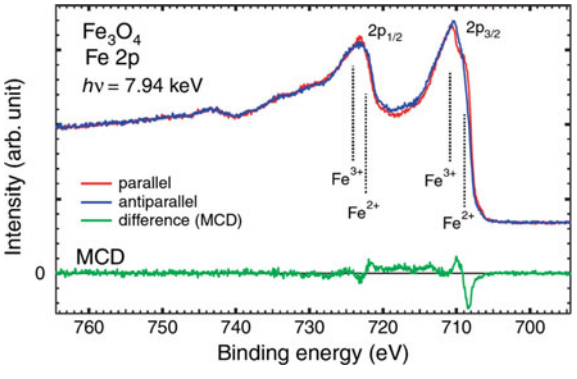

Fig. 1.11 Hard X-ray photoemission MCD (*PMCD*) for Fe 2p core-level emission from a 10 nm-thick Fe_3O_4 film. Data from SPring-8 (From [57])

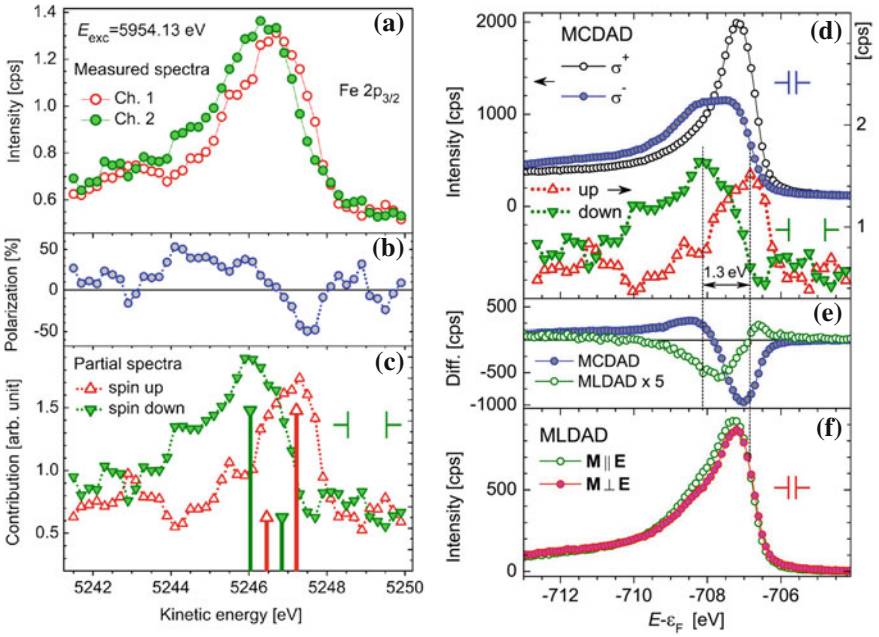

Fig. 1.12 **a**–**c** Spin-resolved spectra and **d**–**e** photoemission MCD (*PMCD*) and MLD (*PMLD*) from Fe $2p_{3/2}$ in a buried layer of $Co_2FeAl_{0.5}Si_{0.5}$ with 5.9 keV excitation. **a** Count rates in spin detector channels, **b** spin polarization derived from the curves in (**a**), and **c** spin-resolved spectra. **d**–**f** Comparison of spin-resolved Fe $2p_{3/2}$ spectra with (**c**) PMCD and (**d**), (**e**) PMLD from the same sample. Data from SPring-8 (From [58])

facilities at present. Thus, an exciting element of future studies will no doubt involve more use of spin resolution.

1.2.8 Photoelectron Diffraction

X-ray photoelectron diffraction (XPD) in core-level emission is a well-developed technique for determining local atomic structure in an element-resolved way, with over 50,000 citations in a Web of Science search based on "photoelectron diffraction". Various reviews of XPD making use of soft X-ray excitation have appeared in the literature [64–66]. In the chapter by Chambers, he illustrates the use of XPD for characterizing oxide heterostructures. The literature on hard X-ray photoelectron diffraction is much more limited, but growing, very much due to Kobayashi et al. [67].

An initial theoretical study [68] of HXPD pointed out that the traditional multiple-scattering cluster model for calculating XPD, as for example, used in the online Electron Diffraction in Atomic Clusters (EDAC) program [69] may not be the most rapidly convergent for HXPD, in which a larger no. of atoms contribute

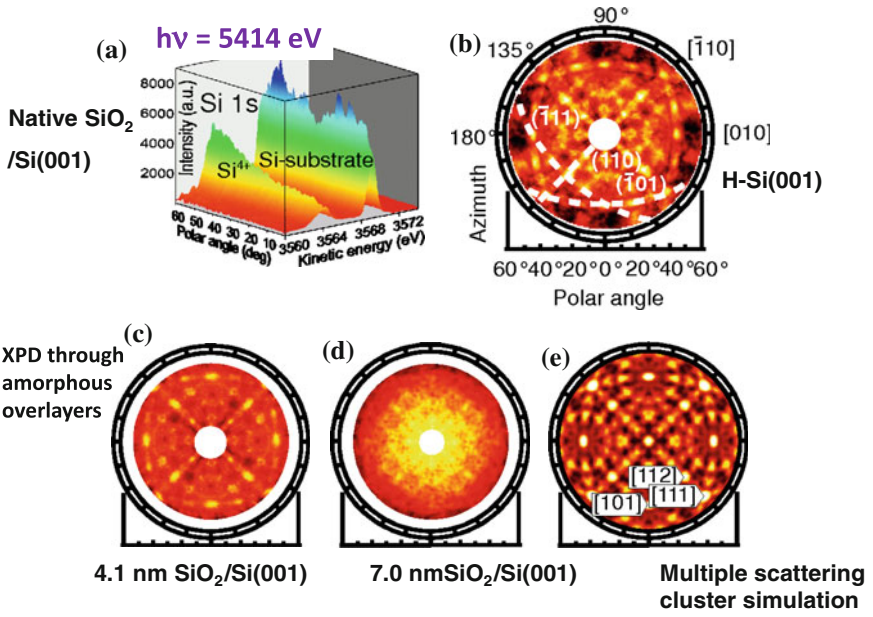

Fig. 1.13 Hard X-ray photoelectron diffraction from Si with varying thicknesses of SiO_2 on top and an excitation energy of 5414.7 eV from a monochromatized laboratory Cr $K\alpha_1$ source. The spectrometer here accepted a very wide angle of $\sim\pm40°$. **a** Si 1s spectra from a Si(001) single-crystal covered by a SiO_2 layer recorded at a certain azimuth. Note the single-shot ability to do ARXPS for depth profiling. **b–d** Two-dimensional HXPD patterns of Si 1s at a kinetic energy of 3569 eV from a Si crystal **b** terminated by H, **c** covered by a 4.1-nm-thick SiO_2 layer and **d** covered by a 7.0-nm-thick SiO_2 layer. The *dashed lines* in **b** indicate Kikuchi bands along the (110) and (111) planar directions. **e** A calculated pattern from a multiple-scattering cluster calculation. Data from a laboratory HXPS system (From [34])

due to the larger IMFPs, and the individual electron-atom scattering events become much more forward peaked, with these combined effects leading to diffraction patterns more properly interpreted as overlapping Kikuchi bands [68]. Thus, a dynamical diffraction approach is more appropriate in the high-energy limit. This prior study pointed out the possible sensitivity of HXPD to the site type of an atom, e.g. as a dopant, and this is a promising future direction for its application. One preliminary study of this type has been done, for Mn in GaAs [70].

As an example of HXPD results, Fig. 1.13 shows some data from Si with various thicknesses of SiO_2 on top, as obtained from a laboratory system using Cr Kα excitation at 5.4 keV [71]. Here, the data are compared to cluster calculations. It is evident that the amorphous SiO_2 overlayer attenuates and smears out the HXPD modulations, but that they are still present to some degree even with 7 nm of amorphous SiO_2 on top. A much more detailed set of such data for ZnO, as compared to both cluster and dynamical diffraction theory, is presented in Fig. 18.28 of the chapter by Kobayashi.

It is thus clear that HXPD will be a very useful aspect of future studies of any single-crystal or epitaxial, or even azimuthally textured, sample, with spectrometers of extremely wide angular acceptance now permitting very rapid data accumulation [71].

1.2.9 Time-Resolved Hard X-ray Photoemission

Another exciting future direction for HXPS is in the ultrafast domain, in which processes on electronic timescales of femtoseconds can be studied. New X-ray free-electron lasers (FELs) with harmonics in the several hundred eV to several keV range are beginning to provide such an opportunity, e.g. at SACLA of SPring-8, the XFEL of DESY, and the LCLS-2 project of SLAC.

Critical in such studies with any FEL is that the space charge of low-energy secondaries above the surface does not cause unacceptable peak shifts or broadenings in spectra, but by now, combinations of experimental data and detailed theoretical modeling have led to readily employable criteria for attenuating the peak flux on the sample so as to control these [72, 73]. Recently, IR-pump/X-ray probe time-resolved photoemission spectra have been obtained at SACLA with 8 keV excitation for V 1s emission from VO_2 and Ti 1s emission from $SrTiO_3$, in what has been called trHAXPES [73]. Essential for the practical future feasibility of such experiments is increasing the pulse frequency by two orders of magnitude or more, such that the peak flux in each pulse can be reduced below the space-charge threshold, while still being able to obtain spectra in a reasonable amount of time. As one possible example of what might be looked at in the time domain, it has been pointed out that the screening of hole states involved in core emission could exhibit different timescales, in particular for the example of the spin-up and spin-down multiplets of a Gd 4s spectrum in Gd during the ferromagnetic to paramagnetic transition [74], but with many other types of screening satellite, as for example that in the Mn 2p spectrum of Mn-doped GaAs in Fig. 1.8, also being candidates for this type of time-resolved measurement.

A second possibility in the time domain involves soft- or hard-X-ray excitation of photoelectron holography from oriented gas-phase molecules, in order to produce so-called “molecular movies” of dissociation or reaction, as has been proposed recently [75, 76].

The future prospects for such time-resolved studies are discussed in much more detail in the chapter by Rossnagel et al., and it is clear that this represents an exciting future dimension in hard X-ray photoemission.

1.2.10 Hard X-ray Photoelectron Microscopy

Adding lateral resolution to HXPS measurements promises to yield a truly three-dimensional picture of a sample, including the added depth penetration for studying multilayer structures and device prototypes. One approach being pursued

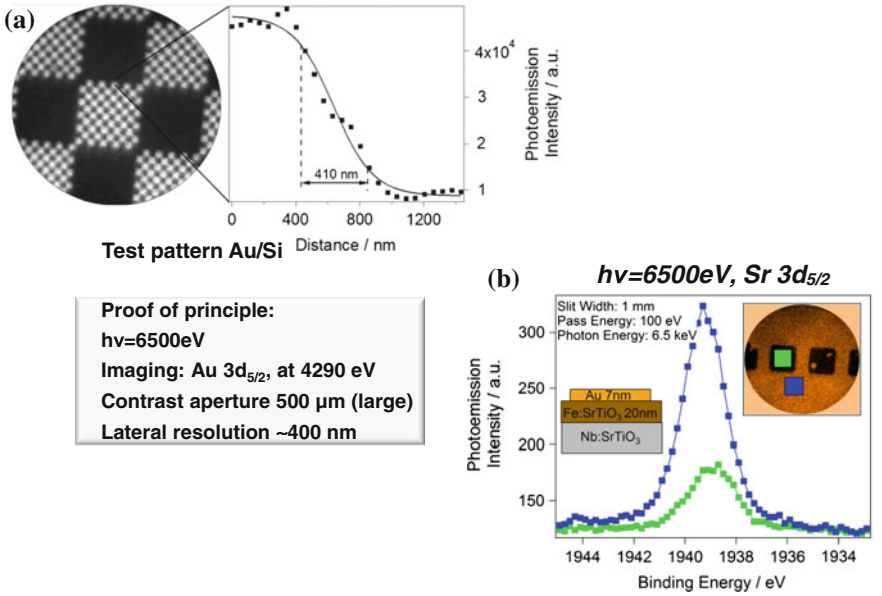

Fig. 1.14 Hard X-ray photo electron microscopy (*HAXPEEM*). **a** *Left* A Au/Si calibration sample imaged on the Au $3d_{5/2}$ photo emission line at a kinetic energy of 4290 eV. *Right* A line scan across a square edge and a 16/84 % profile fit, indicating a resolution of about 400 nm. **b** Selected area hard X-ray photoemission spectra from a patterned Au/$SrTiO_3$ sample, with cross section shown in the *left inset*. Definition of regions of interest in the *right inset*. Data from Petra III (From [77, 78])

in this is to use the electron optical system of a specially-modified photoelectron microscope (PEEM) to yield what has been termed HAXPEEM [77, 78]. Some first results from this approach are shown in Fig. 1.14, where 1.14a shows an image of a reference checkerboard Au–Si pattern that has been used to determine the resolution at 6500 eV photon energy of ~400 nm, and 1.14b shows energy-resolved Sr 3d spectra from an Fe-doped $SrTiO_3$ layer on which a 70 nm thick pad of Au has been grown. Figure 1.14b thus demonstrates that lateral and element-specific resolution is possible through the thick Au overlayer. From an electron optical point of view, it should be possible to improve the resolution into the ~100 nm regime in the future. A wide range of applications of HAXPEEM at this sub-micron resolution level should be possible [78].

An additional useful dimension to HAXPEEM, could be using standing-wave excitation to enhance depth resolution, as demonstrated already with soft X-ray excitation [79, 80], and discussed in a separate section below.

The chapter by Browning discusses this and other possible methods of achieving lateral resolution in hard X-ray photoemission.

1.3 Standing-Wave and Near-Total-Reflection Measurements

1.3.1 Introduction

In this section, the use of various X-ray optical effects to tailor the form of the X-ray wavefield depth distribution so as to achieve greater depth resolution in studies of buried layers or interfaces is discussed. This will involve both the creation of standing waves (SWs) and the concentration of the wavefield near the surface in going into the near-total-reflection (NTR) regime. SW hard X-ray photoemission is discussed in the chapter by Zegenhagen, Lee, and Thiess for the specific case of Bragg reflection from crystal planes, so the focus here will be on Bragg reflection from macroscopic multilayer structures.

In either core-level or valence-level studies in the DOS limit, the basic variation of photoelectron intensity is given by (1.1) or (1.2) respectively, where it is the spatial variation of the X-ray wavefield intensity $I_{hv}(x, y, z, \hat{\varepsilon})$ that is altered through X-ray optical effects. For SW studies this is done principally by varying the incidence angle or photon energy relative to the Bragg condition for a set of Bragg planes in a crystal or a multilayer heterostructure, or a sample grown on a suitable multilayer. This acts to sweep the SW by one half of its intensity period λ_{SW} in a direction perpendicular to the reflecting planes, the z coordinate in Figs. 1.4 and 1.15. As noted from the equations in this figure, the SW period is very close to the period of the multilayer d_{ML}, regardless of the X-ray wavelength = $\lambda_{hv} \equiv \lambda_x$, thus providing a sort of "sub-nm ruler" as the SW is scanned vertically through the sample. For NTR studies, enhanced depth probing is achieved by sweeping the incidence angle from somewhat above the critical angle θ_{crit} at which significant reflection begins to occur to a cutoff angle at which all intensities go to zero. An NTR scan also can involve buried-interface reflections if the critical angles for interfaces above them are larger, and thus SW creation, so the SW and NTR methods have overlapping strengths in providing depth resolution through the analysis of such effects.

1.3.2 Standing-Wave Hard X-ray Photoemission from Multilayer Reflections

Figure 1.15 illustrates the SW method for the case of X-ray Bragg reflection from a multilayer sample, including the two methods mentioned above for scanning the SW through the sample, as well as a third in which one layer of the sample is grown in a wedge form, the incidence angle is held fixed at the Bragg angle, and the SW can be moved through the sample simply by scanning the X-ray beam spot along the slope of the wedge [59]. This type of measurement has been reviewed elsewhere [19, 20, 81, 82].

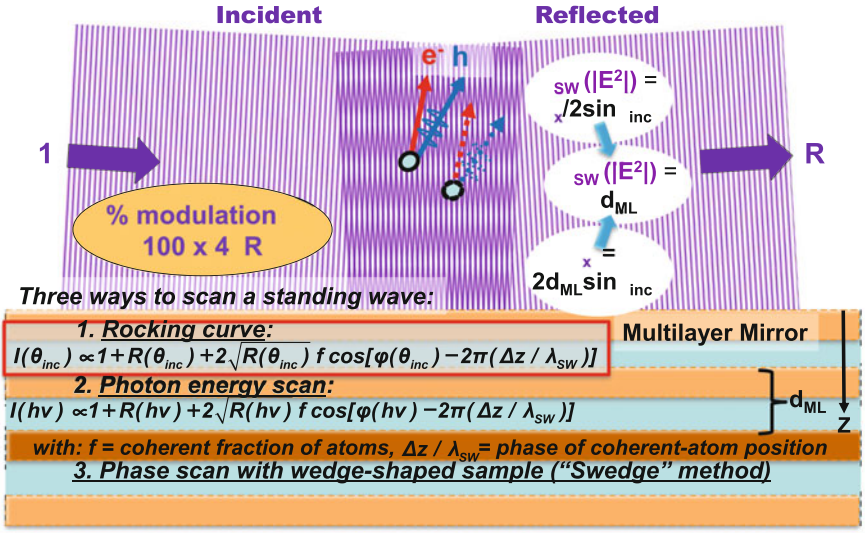

Fig. 1.15 Schematic illustration of the formation of a standing wave (*SW*) in first-order Bragg reflection from a multilayer mirror, together with the equations leading to the standing wave period $\lambda_{SW} \approx$ the multilayer period d_{ML}. The standing wave can be scanned through the sample, which might be the mirror, or grown on top of the mirror, in the three ways indicated: an angle scan or rocking curve, a photon energy scan, or a wedge scan. The equations describing the intensity of the SW are also indicated. (From [19])

The basic physics of creating a standing wave in Bragg reflection from crystal planes is discussed in the chapter by Zegenhagen, Lee, and Thiess, including various applications of this very promising type of measurement, so will not be considered further. However, it is important to note that, for the case of reflection from the nm-scale layers to be considered here, the different materials can be described by a macroscopic index of refraction $n = 1 - \delta - i\beta$, in which β represents absorption and is directly related to the X-ray exponential attenuation length $\Lambda_{hv} = \lambda_{hv}/4\pi\beta$, $\theta_{crit} = sqrt(2\delta)$ for a surface in contact with vacuum, and the wavefield can be calculated by repeatedly applying the Fresnel equations to each significant material interface, including all effects of multiple scattering at these interfaces. This type of calculation is described in detail elsewhere, including a specially written program Yang X-ray Optics (YXRO) that can compute both photoelectron and X-ray emission intensities using (1.1) and is available for online use [83].

A number of soft-X-ray studies have been published using the SW-multilayer method, including overviews [19, 20, 81, 82], and in which the technique has been applied to TM oxide heterostructures [84–86] and magnetic multilayer structures related to spintronics[59, 60, 87, 88], but the focus here will be on examples involving hard X-ray excitation [19, 20, 84, 86–89].

In one particularly illustrative multilayer SW study, a sample consisting of repeated $SrTiO_3$ and $La_{0.7}Sr_{0.33}MnO_3$ bilayers was studied, with rocking curve

measurements being performed on core levels of all of the atoms present, including surface C-containing contaminants. The multilayer was composed of 48 [84] (or in another study 120 [86]) bilayers consisting of alternating 4 unit cells of the band insulator $SrTiO_3$ and 4 unit cells of the half-metallic ferromagnet $La_{0.7}Sr_{0.3}MnO_3$. Both non-resonant hard X-ray excitation at 5950 eV (SPring-8) and resonant soft X-ray excitation at 833.2 eV (ALS) near the La $3d_{5/2}$ absorption edge that maximizes reflectivity were used. The sample configuration and experimental geometry are shown in Fig. 1.16a. The detailed analysis of these RC data appears elsewhere, but as some indication of the effects seen, Fig. 1.16b shows the final results of fitting X-ray optical calculations based on the YXRO program [83] to the experimental rocking curves for all elements. Note the presence of both the primary Bragg reflection rocking curve from the multilayer period d_{ML}, and the Kiessig fringes associated with reflection from the top and bottom of the multilayer stack over a distance D_{ML} (as illustrated in Fig. 1.16a). Theory clearly describes this data, including both types of features, extremely well, and the resulting structure of the multilayer so derived is shown in Fig. 1.16d. Notable here is that it was also found that the multilayer period varied continuously from top to bottom, by about 6 % only, as indicated in Fig. 1.16c, and a subtle structural element thus was cleanly resolvable via this SW analysis. This structural conclusion was also subsequently

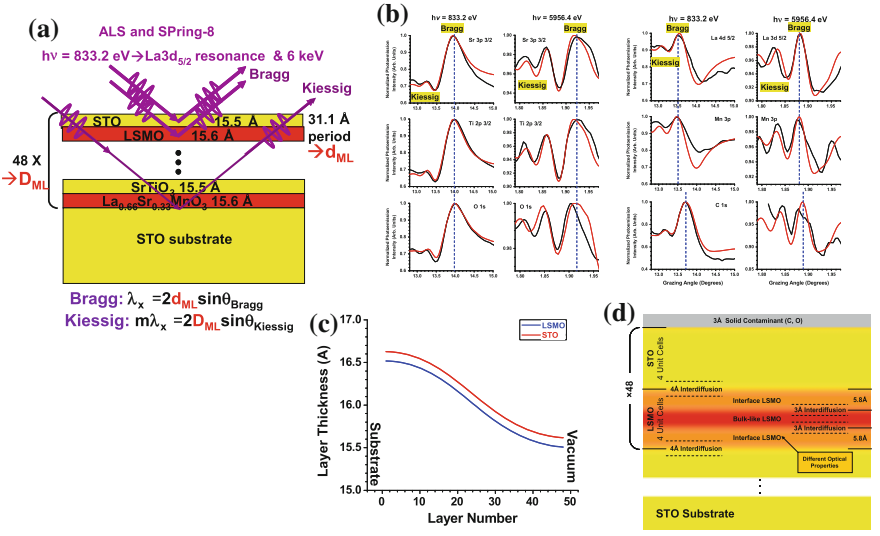

Fig. 1.16 **a** A 48-bilayer multilayer of $SrTiO_3/La_{0.7}Sr_{0.3}MnO_3$ studied with both soft X-ray and hard X-ray standing wave photoemission, with conditions for both 1st-order Bragg and mth-order Kiessig reflections indicated. **b** Results of an X-ray optical analysis of both soft and hard X-ray rocking curves of core-level intensities from all elements in the sample, with the final best-fit to theory being for a multilayer period d_{ML} that changes about 6 % with depth as shown in (**c**), and with interface concentration/roughness profiles as in (**d**). The results in (**c**) and (**d**) have also recently been quantitatively confirmed by TEM/HAADF/EELS (From [84, 86])

confirmed by transmission electron microscopy with energy loss spectroscopy [86]. The soft X-ray core-level spectra also finally revealed an interface binding energy shift for Mn 3p, but not Mn 3s, that can be explained via a crystal-field distortion near the interface [84].

Similar multilayer SW studies with hard X-ray excitation have also been carried out on spintronic systems consisting of MgO on Fe [87] and MgO on FeCoB [88] and a semiconductor system of TiN layer grown on top of a Si/Mo multilayer mirror [89]. In these studies also, subtle chemical shifts of core levels were seen as the SW scans through a buried interface.

It is thus clear that such multilayer SW measurements with hard X-ray excitation can provide unique types depth-resolved information concerning buried layers and interfaces, with a broad range of future applications.

1.3.3 Hard X-ray Photoemission at Near Total Reflection

Beyond these Bragg-reflection standing-wave effects are making use of those which occur as the incidence angle is tuned into near total reflection (NTR), with this possessing the advantage that it can be applied to any material, but in particular, simpler bilayer or trilayer samples that are easier to grow. This type of measurement was stimulated by a pioneering X-ray optics study by Henke [90], followed by experiments involving depth profiles of concentrations [91, 92], with much later studies further developing the method, and pointing out some general advantages of this approach (lower inelastic backgrounds, tunable surface sensitivity, use of Kiessig interference fringes) [93–95]. The terms grazing incidence XPS (GIXPS) or total reflection XPS (TRXPS) have been used in these studies, but NTR will be used here.

An updated application of this NTR approach is shown in Fig. 1.17, which presents some HXPS experimental data and theoretical calculations for a bilayer sample of ferroelectric $BiFeO_3$ on top of a Ce-doped Mott insulator ($Ca_{0.96}$, $Ce_{0.04}$) MnO_3 (BFO on CCMO) [96], a system recently studied as leading to strong ferroelectric control of the Mott insulator transition in the 2D electron gas at the interface between them [97]. The photon energy was 2.8 keV. The intensities of various core level intensities have been monitored as a function of incidence angle : C 1s from the surface contaminant overlayer, Bi 4f from BFO, and two components of Ca 2p from CCMO that are clearly resolved in the spectra of Fig. 1.17a, obtained at angles for which the calculations of electric field intensity in Fig. 1.17b for the final optimized sample geometry in Fig. 1.17c indicate enhanced sensitivity to the BFO/CCMO interface (higher binding energy) or the bulk of the CCMO (lower binding energy). The angular-dependent raw data for these four intensities are shown in Fig. 1.17d, and they clearly show differences in both the final decrease to zero at total reflection and the oscillatory standing-wave interference phases seen for higher angles. Noteworthy in Fig. 1.17d is the systematic change in the low-angle cutoff for atomic species at different depths, a generally useful effect even at this qualitative level. The comparison of theory for the optimized sample

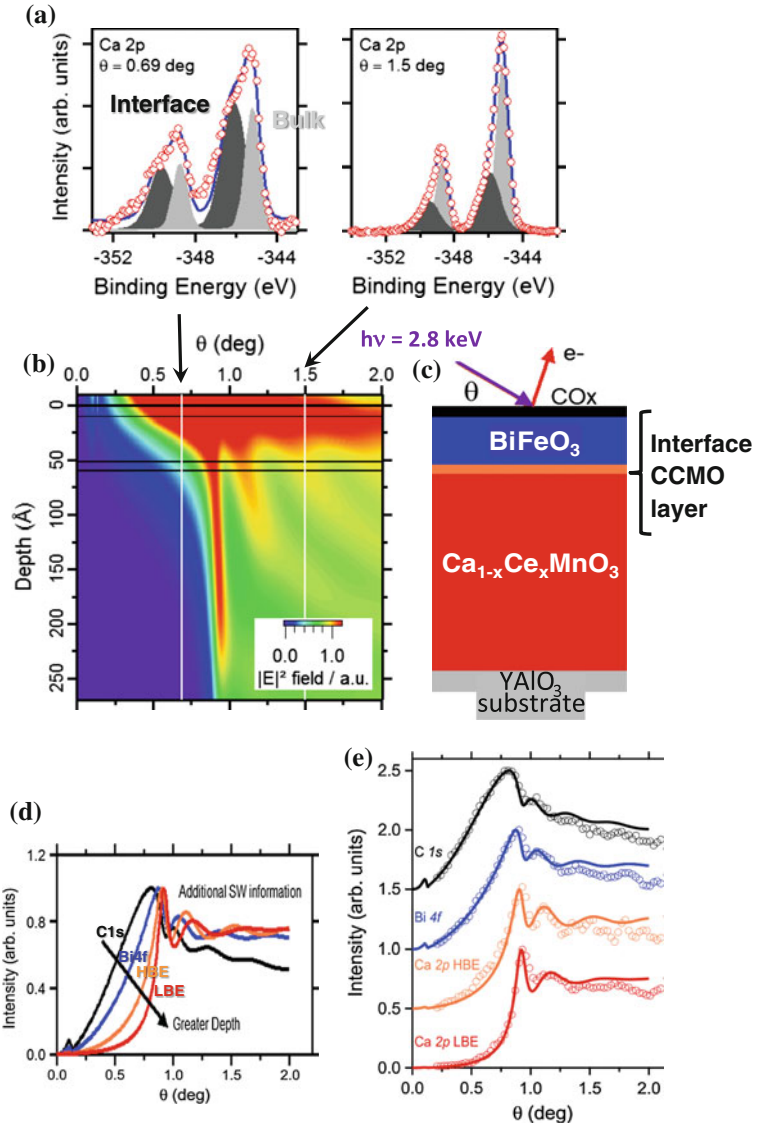

Fig. 1.17 Using near total reflection (*NTR*) HXPS on a complex oxide system, for a bilayer of $BiFeO_3$ and Ce-doped $CaMnO_3$, grown on an $YAlO_3$ substrate. **a** The Ca 2p spectra at two incidence angles emphasizing the high-binding-energy (interface) and low-binding-energy (bulk) CCMO regions. **b** The calculated electric field strength as a function of depth and incidence angle for the sample configuration in (**c**), which was derived by fitting X-ray optical theory to Ca 2p, Bi 2p, and C 1s intensities as a function of angle. **d** The experimental intensity variation of C 1s, Bi 4f, HBE Ca 2p and LBE Ca 2p with incidence angle over the NTR region. **e** The optimized final fits of X-ray optical calculations to the data in (**d**), for the sample configuration in (**c**). Data from the ALS (From [96])

geometry and experiment in Fig. 1.17e further shows excellent agreement, and the ~10 Å thickness of the 2DEG in the CCMO associate with the higher-binding energy Ca peak derived by fitting the NTR experiment to theory agrees well with a separate analysis of small shifts in TEM-EELS Mn-L_3 near-edge features, further confirming the utility of NTR photoemission in buried interface studies. The oscillations here are due to reflections and interference at the surface and the two buried interfaces in the sample, and the peaks in intensity near 0.9° to the spreading of the X-ray beam along the spectrometer entrance slit direction and the concentration of electric field near the surface, the latter an effect first observed and explained by Henke [90]. Important additional features are the differences in phase of the oscillations for Bi and Ca shown in Fig. 1.17d, which are useful through the process of optimizing the sample geometry to fit experiment in deriving depth-dependent interface information for this and other similar future samples.

Such NTR measurements thus represent another promising direction for buried interface and buried layer characterization with HXPS.

1.4 Valence-Level Studies, Including Angle-Resolved Photoemission

Valence-level studies using conventional XPS or HXPS have almost all been carried out in the MEWDOS or XPS limit, in which very useful information on momentum-integrated electronic structure can be obtained, and several such studies are reviewed in the chapters by Kobayashi and Tjeng. Such data, which will always be at higher energy and/or temperature, can often be fruitfully analyzed using (1.2), as discussed for example in prior single-crystal Bragg-reflection standing-wave work by Woicik et al. [98–101], and in the chapter by Zegenhagen, Lee, and Thiess.

However, interest is growing in doing more bulk sensitive momentum-resolved ARPES in both the soft X-ray (SARPES) and hard X-ray (HARPES) regime, for several reasons reviewed elsewhere [18–20, 102]. Momentum resolution in this context refers to so-called direct transitions (DTs) from $\vec{k}_i$ to $\vec{k}_f$ according to $\vec{k}_i = \vec{k}_f - \vec{k}_{hv} - \vec{g}_n$, where $\vec{k}_{hv} = 2\pi\nu/c$ is the photon wave vector and $\vec{g}_n$ is the relevant reciprocal lattice vector, and the low-energy ARPES version of this equation of $\vec{k}_i = \vec{k}_f - \vec{g}_n$ has been modified to allow for the photon momentum because of effects beyond the dipole approximation, as discussed also in an earlier section. For a given experimental geometry, this non-dipole correction is easily made.

Gray et al. first showed that momentum-resolved ARPES is possible with hard X-ray excitation, for the examples of W at 6 keV, and GaAs plus Mn-doped GaAs at 3.2 keV [39, 40], thus providing a novel probe of truly bulk electronic structure. Such HARPES measurements are reviewed in detail in the chapter by Gray, and certainly represent a promising future direction in HXPS studies.

The data analysis of HARPES, and its theoretical interpretation, must allow for the momentum-smearing effects of phonon creation and annihilation, as estimated

e.g. through the Debye-Waller factors of Fig. 1.9a. Simple first-order correction procedures to experimental data for both phonon and HXPD effects are discussed elsewhere [39, 40]. The most quantitative theoretical interpretation of HARPES is via the so-called one-step or "time-reversed LEED" method that has been used in prior studies, as pioneered by Gray et al. [39, 40]. This method has furthermore been improved to include phonon effects more precisely in recent work [103], and is discussed in more detail in the chapter by Braun, Ebert, and Minar, with phonon effects discussed in connection with their Figs. 7.1 and 7.2.

I will here focus only on an additional possible dimension of such HARPES measurements in which a single-crystal Bragg reflection is used to create a standing wave that is scanned perpendicular to the set of $hk\ell$ planes responsible for the reflection. This is thus the same sort of experiment discussed in the chapter by Zegenhagen, Lee, and Thiess, but with the addition of momentum resolution. The goal is thus to determine electronic structure that is both element- and momentum resolved. The SW wavelength is now given by $d_{hk\ell}$, the spacing between these planes, and the scanning is here done through the second method indicated in Fig. 1.15, that is, by scanning the photon energy through the Bragg condition.

As a first indication of the feasibility of such SW-HARPES, some encouraging proof-of-principle results results have been obtained recently for the systems of GaAs(001) and (Ga,Mn)As(001) (two materials studied previously with HARPES in [39, 40]), using an HXPS facility especially suited for this at Diamond [104]. Some of these results are summarized in Fig. 1.18. In Fig. 1.18a, very broad angular range single-detector HARPES images (cf. Fig. 1.2) for $Ga_{0.95}Mn_{0.05}As$ and GaAs, obtained near the (311) reflection from (001)-oriented surfaces with a photon energy of about 3650 eV, are compared. The entire VB spectrum in energy is probed, and over about 7 BZs in momentum. There are conspicuous differences between the undoped and doped samples: a general smearing of features in the doped sample, as seen previously over a much more limited BZ range [39, 40], but also and more significantly, enhanced intensities in the doped sample at several specific points, as circled in yellow, including in particular what is interpreted as a Mn-induced impurity band near the Fermi energy (E_F). In Fig. 1.18b, SW photon energy scans of the Ga 3d, As 3d and Mn 2p intensities from the doped sample over the (311) reflection are shown, with clear evidence of separate Bragg reflections from both the substrate GaAs (the sharper features) and the doped layer (the broader features), separated by a few eV due to slightly different lattice constants, and broader for the doped layer due to its finite thickness of only $\sim$100 nm, compared to the GaAs substrate. In addition, the Ga and Mn curves are essentially identical, clearly indicating that the Mn occupies substitutional, rather than interstitial, sites. These two curves are furthermore different from that of As, due to the difference in position in the unit cell.

Going further, core-level SW energy scans such as those in Fig. 1.18b, obtained simultaneously with HARPES results in similar small energy steps over the substrate Bragg features, can be used to project the HARPES images onto the atomic makeup at each point in binding energy and $\vec{k}$. This proceeds based on the use of (1.2), as

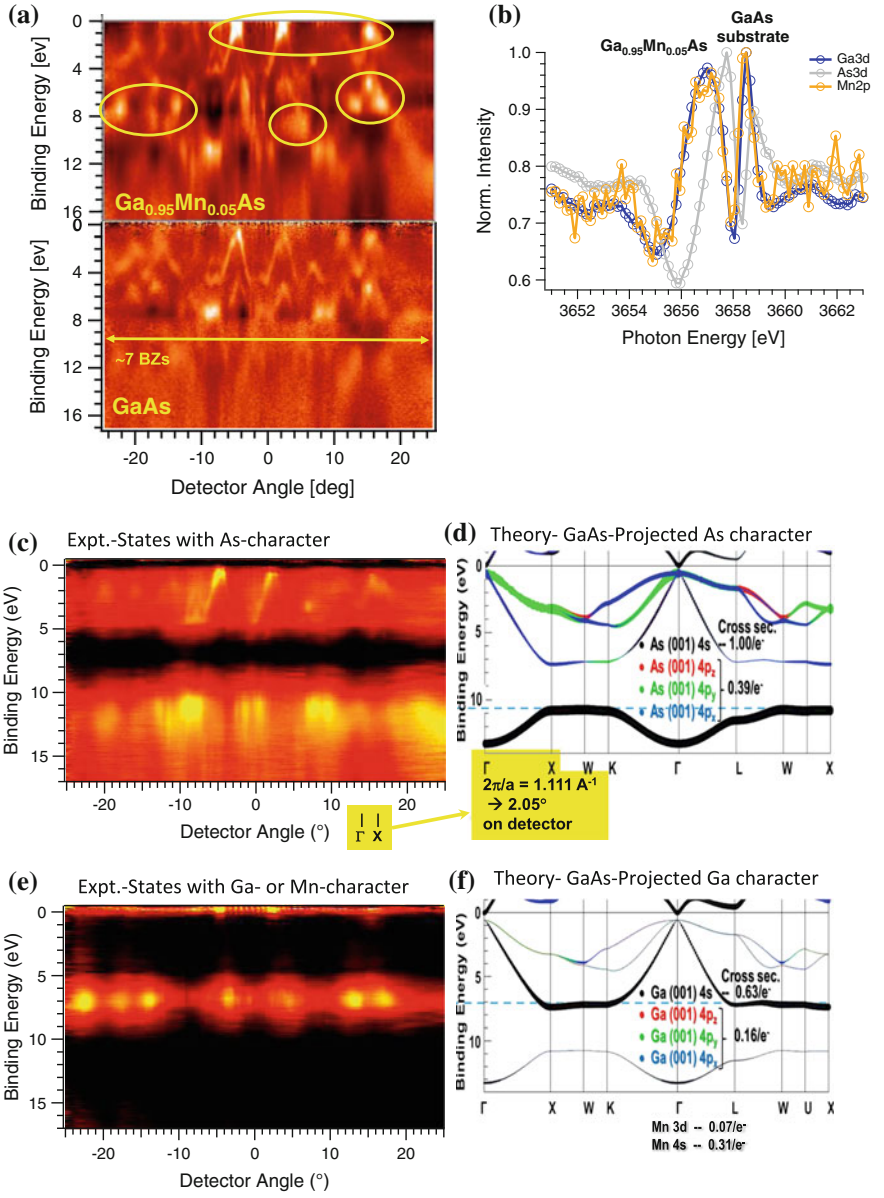

Fig. 1.18 Standing-wave HARPES based on crystal Bragg reflection. **a** HARPES results for $Ga_{0.95}Mn_{0.005}As$ and undoped GaAs, with *circled* features that are strongly enhanced for the dilute magnetic semiconductor (*DMS*). Approximately 7 Brillouin zones are sampled. **b** A photon-energy scan of Ga 3d, As 3d, and Mn 2p intensities through the (311) reflection for $Ga_{0.95}Mn_{0.05}As$, exhibiting two separate Bragg reflections, as indicated. **c** and **e** Orbital-projected standing-wave HARPES results for As and Ga + Mn, respectively, based on the core-level photon energy scans from $Ga_{0.95}Mn_{0.05}As$ in panel (**b**). For the mean exciting energy of hν = 3657 eV, the photoelectron wave vector is k_f = 30.96 $Å^{-1}$, and the resulting Γ-X distance along the detector in degrees is indicated. **d** and **f** Orbital-projected LDA band structures for As and Ga respectively, from [39] and [40], with the Γ-X distance for GaAs again indicated. Data from Diamond (From [104])

done in previous studies at the MEWDOS limit [99], and the additional assumption that the core-level scans are representative of the SW form at each atom, such that each pixel is a linear superposition of intensities from As and Ga(Mn)

$$I_{HARPES}(E_B, \vec{k}, hv) \approx I_{As}(E_B, \vec{k}, hv) + I_{Ga(Mn)}(E_B, \vec{k}, hv), \tag{1.3}$$

and comparing this equation using a normalized least-squares approach for the full photon energy scan to

$$I_{core}(E_B, \vec{k}, hv) = f_{As}(E_B, \vec{k}) I_{As3d}(hv) + (1 - f_{As}(E_B, \vec{k})) I_{Ga3d(Mn2p)}(hv) \tag{1.4}$$

so as to finally yield f_{As}*and* $f_{Ga} = (1 - f_{As})$ over the full HARPES E_B, $\vec{k}$ image, pixel-by-pixel. The raw data such as that in the top panel of Fig. 1.18a are then multiplied by either f_{As} or f_{Ga}, yielding the results in Fig. 1.18c, e, respectively. These two projected images are markedly different, showing bands of maximum intensity and bands of minimum intensity that are out of phase with one another. Note also the preservation of enhanced Ga- or Mn-character near the Fermi level in Fig. 1.18e due to the Mn impurity band. Since the two atoms Ga and Mn occupy the same site type, we cannot project Mn alone, although some kind of resonant experiment might permit this in the future.

As confirmation that these projected SW-HARPES images are a valid representation of the atom-projected electronic structure, Figs. 1.18d, f show theoretical projected GaAs band structures from the prior HARPES study [39, 40], with the different orbitals involved specified and the thickness of the curve indicating relative population. There is excellent qualitative agreement as to those regions that should exhibit more As character, and those that should exhibit Ga (or Mn) character. The relative size of the Γ-X distance in the BZ between experiment and theory is indicated for reference. An important point in using the above method for analyzing such results that has been mentioned in connection with (1.2) is that it has long been realized through various theoretical studies that the matrix elements and cross sections for valence photoemission are increasingly controlled by the inner spatial regions of each atom involved [26, 27], thus making the use of core-level intensities on the same atom at nearly the same kinetic energy a good approximation for such SW projection procedures.

Although a complex type of measurement requiring special instrumentation and precise sample manipulation, SW-HARPES measurements represent a promising future technique in the study of complex quantum materials.

1.5 Measurements at Higher Ambient Pressures

The chapter by Liu and Bluhm discusses in detail the rapidly growing technique of near ambient- or high-pressure photoemission spectroscopy (APPS, APXPS, APPES, HPPES, NAP-XPS,…) [105, 106], in which a combination of strong

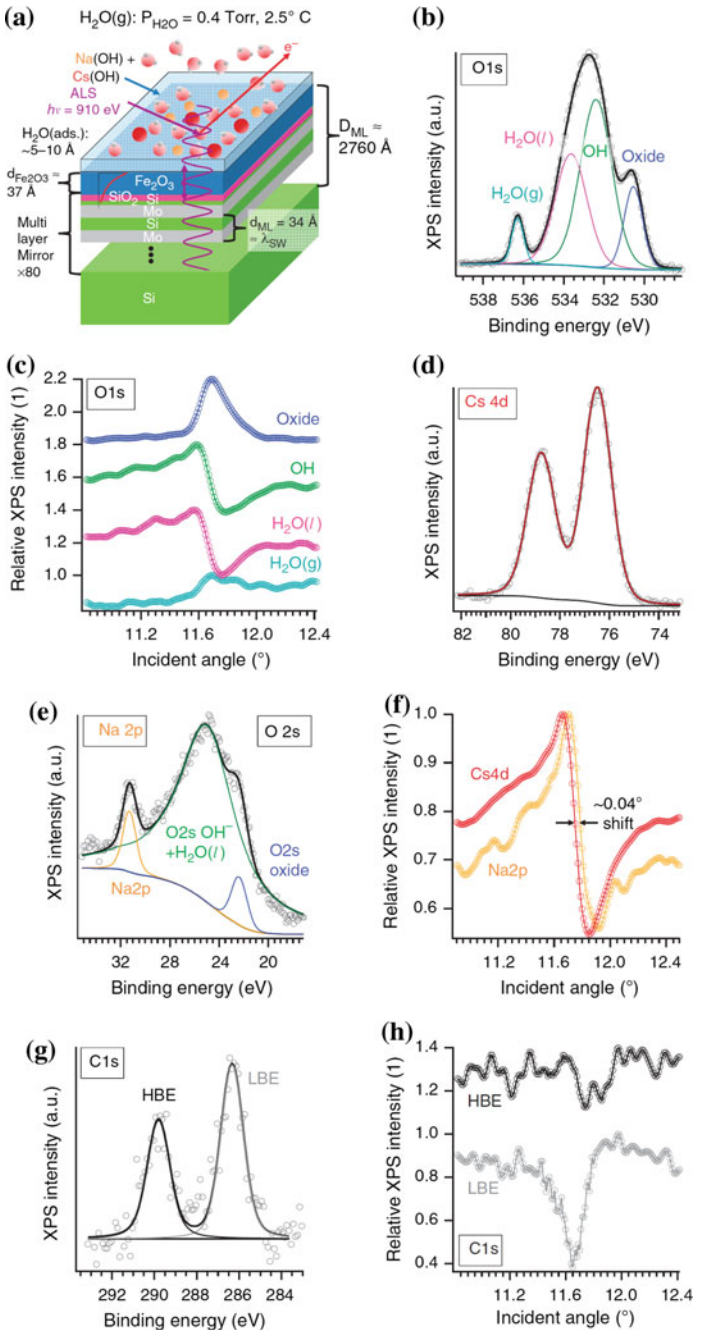
(a)
H2O(g): PH2O = 0.4 Torr, 2.5° C
Na(OH) +
Cs(OH)
ALS
hν = 910 eV
e−
H2O(ads.):
~5–10 Å
DML ≈
2760 Å
dFe2O3 ≈
37 Å
Fe2O3
SiO2
Si
Mo
Si
Mo
dML = 34 Å
≈ λSW
Multi
layer
Mirror
×80
Si
(b)
O1s
XPS intensity (a.u.)
H2O(l)
OH
Oxide
H2O(g)
538 536 534 532 530
Binding energy (eV)
(c)
O1s
Relative XPS intensity (1)
2.2
2.0
1.8
1.6
1.4
1.2
1.0
Oxide
OH
H2O(l)
H2O(g)
11.2 11.6 12.0 12.4
Incident angle (°)
(d)
Cs 4d
XPS intensity (a.u.)
82 80 78 76 74
Binding energy (eV)
(e)
Na 2p
O 2s
XPS intensity (a.u.)
O2s OH−
+H2O(l)
O2s
oxide
Na2p
32 28 24 20
Binding energy (eV)
(f)
Relative XPS intensity (1)
1.0
0.9
0.8
0.7
0.6
Cs4d
~0.04°
shift
Na2p
11.2 11.6 12.0 12.4
Incident angle (°)
(g)
C1s
XPS intensity (a.u.)
HBE
LBE
292 290 288 286 284
Binding energy (eV)
(h)
Relative XPS intensity (1)
1.4
1.2
1.0
0.8
0.6
0.4
HBE
LBE
C1s
11.2 11.6 12.0 12.4
Incident angle (°)

◀ **Fig. 1.19** Combining standing-wave and ambient-pressure photoemission (SWAPPS). **a** The sample configuration, with some relevant dimensions noted. **b** An O 1s spectrum, resolved into four unambiguous components by peak fitting of the rocking curves for this spectrum. **c** The rocking curves for the four types of oxygen indicated in (**b**). **d** and **e** The Cs 4d spectrum and analogous overlapping Na 2p and O 2s spectra, with peak fitting. **f** The rocking curves for Cs 4d and Na 2p derived from spectra such as those in (**d**) and (**e**). **g** A typical C 1s spectrum, showing the two components, one at low binding energy (*LBE*) and one at higher binding energy (*HBE*). **h** The rocking curves for the two C 1s components. Data from the ALS (From [107])

differential pumping and special electron optics in the entry lens to a hemispherical analyzer is used to permit going to pressures at the sample surface that are now up to 20 Torr, with future projections to much higher values. Thus, much more realistic measurements can be made of various important surface reactions in catalysis, corrosion, environmental science, and many other areas of science and technology.

I will thus not comment in detail on APPS, but simply point out a recently developed connection to the standing-wave technique mentioned above in what has been termed SWAPPS [107, 108]. This first application of SWAPPS used soft X-ray excitation and was to a liquid-like $\sim$1 nm thick aqueous film containing NaOH and CsOH on a surface of Fe_2O_3 hematite, grown on a Si/Mo soft X-ray mirror as the SW generator, as illustrated in Fig. 1.19a. Rocking curves were measured for the core-level intensities from all of the species present, including four types of oxygen and gas-phase water above the surface, which could be resolved due to chemical shifts, as shown in Fig. 1.19b. In Fig. 1.19c, it is remarkable that all four oxygen components show the effects of the SW scanning through the surface, including even the gas-phase water, and that they each have distinct shapes, exhibiting also what are found to be Kiessig fringes. Figure 1.19f now compares the rocking curves for Cs 4d and Na 2p, as derived from spectra such as those in Fig. 1.19d, e, and reveals a small but reliable shift of 0.04° in the steeply sloping regions of the two curves near the Bragg angle of the multilayer, but also a different shape in the wings away from these regions, with Cs having higher intensity both below and above the Bragg angle. Figure 1.19g, h further show two different types of contaminant C, at high- and low-binding energy (HBE and LBE), and they have distinctly different rocking curves. Going further, these rocking curves have been compared to X-ray optical calculations while varying the layer thicknesses, positions, and linear interface regions in the sample structure, and the optimum structure as fit to these data, shown in Fig. 1.20i, yields the comparisons shown in Fig. 1.20a–h. Some significant conclusions from this study are thus that Cs and Na do not have the same distribution, but Cs is rather excluded from near the Fe_2O_3-aqueous interface, and that the two C species have very different distributions, with the HBE distributed throughout the full aqueous layer and LBE being limited to a hydrophobic surface film.

Beyond these soft X-ray results, it has also been pointed out that using hard X-ray excitation both permits looking through thicker surface layers at buried interface, and going to higher pressures due to the longer IMFPs of the emitted photoelectrons [11], such that thin liquid films in equilibrium with the electrolyte in

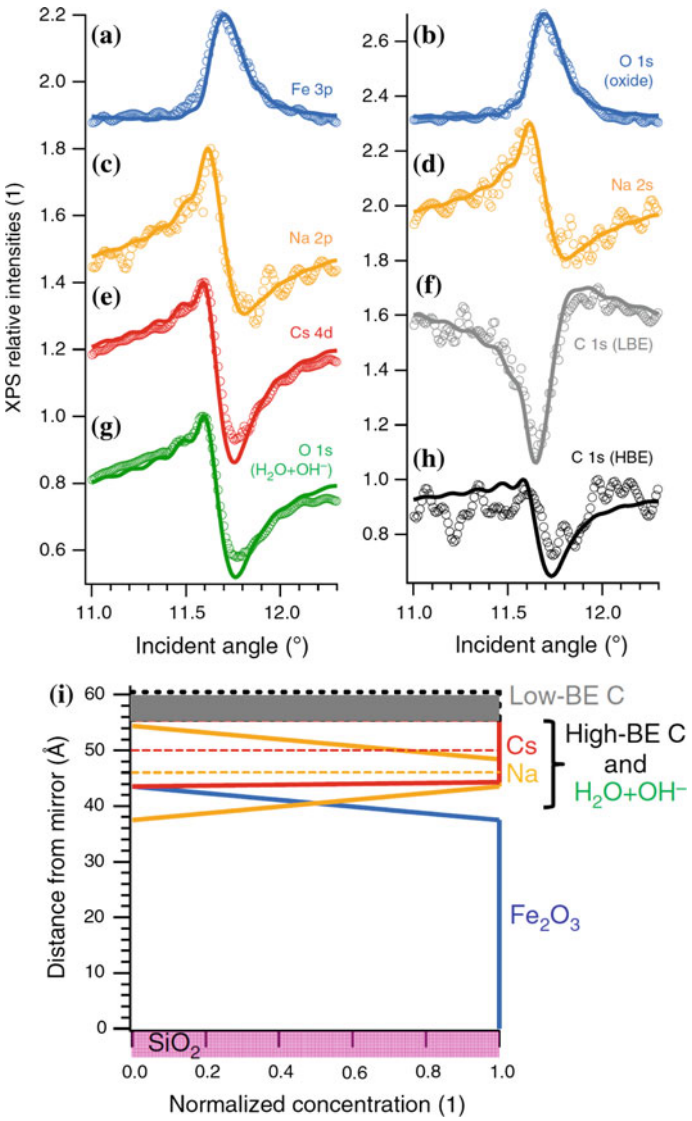

Fig. 1.20 Standing-wave ambient pressure photoemission (SWAPPS). **a**–**h** A comparison of the experimental rocking curves for various core-level intensities with theoretical calculations based on the optimized sample configuration shown in (**i**). **a** Fe 3p, **b** O 1s (oxide), **c** Na 2p, **d** Na 2s, **e** Cs 4d, **f** low binding energy (*LBE*) C 1s, **g** O 1s (OH^- + H_2O), **h** high binding energy (*HBE*) C 1s. **i** The concentration profiles for the optimized sample configuration. Data from the ALS (From [107])

an electrochemical cell can be studied, thus opening up exciting new possibilities in APPS. The combination of hard X-rays and SW excitation has also recently been demonstrated in an electrochemical cell for the first time [108].

These results thus point to the use of hard X-ray SWAPPS measurements for studying the interface region of surface reactions at realistic pressures in a much more precise and both element- and chemical state-resolved way than has previously been possible.

1.6 Concluding Remarks

It is thus clear that hard X-ray photoemission is a rapidly developing and versatile technique, which in fact by now encompasses all of the modalities represented in Fig. 1.2. Its ability to probe more deeply into any condensed matter system leads to an enormous range of applications from complex bulk materials to multilayer nanostructures to *in operando* device prototypes, as amply illustrated by the other chapters in this book. The higher energies involved are also of inherent interest in atomic and molecular studies, again as discussed later in this book.

Some more specific summary comments are: The quantitative analysis of HXPS core and valence data is in several respects simpler, including ARXPS for depth profiling and decomposition of valence spectra into their element-specific components. Adding polarization variation provides additional orbital and magnetic sensitivity. Spin resolution begins to be applied to magnetic systems, with promise of much more efficient detectors in the near future. Hard X-ray photoelectron diffraction (HXPD) provides bulk- and element-sensitive structural information that is qualitatively different from that in the soft X-ray regime, including its connection to Kikuchi bands. The use of standing wave (SW)- and near total reflection (NTR)-measurements yields unique information on buried interfaces and layers. Angle-resolved valence-level studies can also yield momentum-resolved electronic structure through hard X-ray ARPES (HARPES), and perhaps through Bragg-reflection SW excitation both momentum- and element-resolved electronic structure. Ambient pressure photoemission (APPS) benefits from higher energies in attaining higher pressures and penetrating thicker surface films to look at buried interfaces. Finally, combining hard x-ray SW excitation with APPS in SWAPPS shows promise of providing information with unprecedented detail on the solid/liquid interface.

Acknowledgements The work in my group discussed here has been supported by the Director, Office of Science, Office of Basic Energy Sciences, Materials Sciences and Engineering Division, of the U.S. Department of Energy under Contract No. DE-AC02-05CH11231, through the Materials Sciences Division of the Lawrence Berkeley National Laboratory (LBNL), and by the Laboratory Directed Research and Development program of LBNL. Additional support has come from Army Research Office MURI grant W911-NF-09-1-0398 for oxide heterostructure research; from the Jülich Research Center, Peter Grünberg Institute (PGI-6); and from the Labex PALM APTCOM Project of the Triangle de Physique (Paris), No. ANR-10-LABX-0039.

My special gratitude also goes to Alexander X. Gray and Slavomir Nemšák for their significant contributions to much of the recent work described herein, and to S.N. for his assistance in the preparation of this manuscript. I am also grateful to the various co-authors in my group and elsewhere who have contributed so much to our work in HXPS, including various scientists who have provided excellent assistance with measurements at the Advanced Light Source, BESSY, ESRF, Petra III, Soleil, SPring-8, and the Swiss Light Source.

References

1. P. Pianetta, I. Lindau, Nature **250**, 215 (1974)
2. HAXPES03-ESRF, Nucl. Inst. Meth. A **547**, 1–238 (2005)
3. HAXPES06- SPring8, http://haxpes2006.spring8.or.jp/program.html
4. HAXPES-ALS (2008), http://ssg.als.lbl.gov/ssgdirectory/fedorov/workshops/index.html
5. HAXPES09-NSLS, http://www0.bnl.gov/ps/nsls/workshops/2009/haxpes/
6. HAXPES11-DESY (2009), http://haxpes2011.desy.de
7. HAXPES-ESRF (2012), http://www.esrf.eu/files/live/sites/www/files/events/conferences/2012/users-meeting-2012-workshops/xsw-haxpes-workshop/Programme.pdf
8. HAXPES13-Uppsala, http://www2.physics.uu.se/external/haxpes2013/
9. HAXPES15-Taiwan, http://www.nsrrc.org.tw/haxpes-2015
10. HAXPES17-Berkeley, To be held 11–15 Sept. 2017
11. S. Axnanda et al., Sci. Rep. **5**, 09788 (2015)
12. J. Zegenhagen (ed), in Nuclear Instruments and Methods A vol. 547, pp. 24–41 (2005). Papers from First HXPS Conference
13. L. Kover (ed), J. Electron Spectrosc. **178–179**, 1–448 (2010), dedicated issue on XPS and HXPS
14. W. Drube (ed) J. Electron. Spectrosc. **190**, 125–314 (2013), dedicated issue on HXPS
15. C.S. Fadley, Nuclear Instruments and Methods A **547**, 24–41 (2005), special issue edited by J. Zegenhagen, C. Kunz
16. C.S. Fadley, Nucl. Inst. Meth. A **601**, 8 (2009)
17. C.S. Fadley, J. Electron Spectroc. **178–179**, 2 (2010)
18. C.S. Fadley, Synchrotron Radiation News **25**, 26 (2012)
19. C.S. Fadley, J. Electron Spectrosc. **190**, 165 (2013)
20. C.S. Fadley, S. Nemšák, J. Electron Spectrosc. **195**, 409 (2014)
21. S. Tanuma, C.J. Powell, D.R. Penn, Surf. Interf. Analysis **43**, 689 (2011)
22. F. Offi, S. Iacobucci, P. Vilmercati, A. Rizzo, A. Goldoni, M. Sacchi, G. Panaccione, Phys. Rev. B **77**, 201101R (2008)
23. F. Offi, S. Iacobucci, L. Petaccia, S. Gorovikov, P. Vilmercati, A. Rizzo, A. Ruocco, A. Goldoni, G. Stefani, G. Panaccione, J. Phys. Condens. Matter **22**, 305002 (2010)
24. R. Yoshida et al., Physica C **469**, 1034 (2009)
25. W.S.M. Werner, L. Köver, S. Egri, J. Toth, D. Varga, Surf. Sci. **585**, 85 (2005)
26. C.S. Fadley, Basic concepts of X-ray photoelectron spectroscopy, in *Electron Spectroscopy: Theory, Techniques, and Applications*, ed. by C.R. Brundle, A.D. Baker (Academic Press, London, 1978)., vol. II, Chap. 1, pp. 56–57. Available as download from http://www.physics.ucdavis.edu/fadleygroup/BasicConceptsofXPS.pdf
27. C. Solterbeck, W. Schattke, J.-W. Zahlmann-Nowitzki, K.-U. Gawlik, L. Kipp, M. Skibowski, C.S. Fadley, M.A. Van Hove, Phys. Rev. Lett. **79**, 4681 (1997)
28. W. Smekal, W.S.M. Werner, C.J. Powell, Surf. Interface Anal. **3**, 1059 (2005)
29. W.S.M. Werner, W. Smekal, T. Hisch, J. Himmelsbach, C.J. Powell, J. Electron Spectrosc. **190**, 137 (2013)

30. P.H. Scofield, Lawrence Livermore Laboratory Report UCRL-51326 (1973). Available at http://www.physics.ucdavis.edu/fadleygroup/Scofield.CrossSections.UCRL51326.pdf
31. M.B. Trzhaskovskaya, V.I. Nefedov, V.G. Yarzhemsky, At. Data Nucl. Data Tables **77**, 97 (2001)
32. M.B. Trzhaskovskaya, V.I. Nefedov, V.G. Yarzhemsky, At. Data Nucl. Data Tables **82**, 257 (2002)
33. K. Kobayashi et al., Appl. Phys. Lett. **83**, 2005 (2003)
34. I. Piš, M. Kobata, T. Matsushita et al., Anal. Sci. **26**, 227 (2010)
35. J. Buck et al., Proceedings of SPIE **8504**, 85040U (2012)
36. W.Wurth, S. Svensson, N. Mårtensson, private communication
37. J.M. Bussat et al., IEEE Trans. Nucl. Sci. **51**, 2341 (2004)
38. R. Guillemin, O. Hemmers, D.W. Lindle, S.T. Manson, Radiat. Phys. Chem. **75**, 2258 (2006)
39. A.X. Gray et al., Nat. Mater. **10**, 759 (2011)
40. A.X. Gray et al., Nat. Mater. **11**, 957 (2012)
41. A. Sekiyama, New J. Phys. **12**, 043045-1-11 (2010)
42. A. Sekiyama, A. Higashiya, S. Imada, J. Electron Spectrosc. **190**, 201 (2013)
43. S. Goldberg, S. Kono, C.S. Fadley, J. Electron Spectrosc. **21**, 285 (1985)
44. S. Nemšák, N. Kaduwela, C.S. Fadley, Program based on equations from Ref. 32, with beta test version. Accessible at http://.naomi.nocube.sk/; S. Nemšák, private communication
45. J. Weinen et al., J. Electron Spectrosc. **198**, 6 (2015)
46. K. Horiba, M. Taguchi, A. Chainani et al., Phys. Rev. Lett. **93**, 236401 (2004)
47. M. Taguchi et al., Phys. Rev. Lett. **95**, 177002 (2005)
48. J. Fujii et al., Phys. Rev. Lett. **107**, 187203 (2011)
49. M. Van Veenendaal, Phys. Rev. B **74**, 085118 (2006)
50. Y. Takata et al., Phys. Rev. B **75**, 233404 (2007)
51. Y. Takata, Phys. Rev. Lett. **101**, 137601 (2008)
52. S. Suga et al., New J. Phys. **11**, 073025 (2012)
53. Y. Kayanuma, I. Fukahori, S. Tanaka, Y. Takata, J. Electron Spectrosc. **184**, 468 (2011)
54. M. Simon et al., Nat. Comm. **5**, 4069 (2014)
55. C. Papp, L. Plucinski et al., Phys. Rev. B **84**, 045433 (2011)
56. C.M. Schneider, U. Pracht, W. Kuch, A. Chassé, J. Kirschner Phys. Rev. Lett. **54**, R15618 (1996)
57. S. Ueda et al., Appl. Phys. Express **1**, 077003 (2008)
58. G. Stryanyuk et al., Jpn. J. Appl. Phys. **51**, 016602 (2012)
59. S.-H. Yang et al., J. Phys. Cond. Matt. **14**, L406 (2002)
60. S.-H. Yang et al., Phys. Rev. B **84**, 184410 (2011)
61. C. Tusche et al., Appl. Phys. Lett. **99**, 032505 (2011)
62. V.N. Strocov, V.N. Petrov, J.H. Dil, J. Synchrotron Rad. **22**, 708 (2015)
63. C. Joswiak et al., Rev. Sci. Instr. **81**, 053904 (2010)
64. D.P. Woodruff, Rep. Prog. Phys. **57**, 1029 (1994)
65. C.S. Fadley, M.A. Van Hove, Z. Hussain, A.P. Kaduwela, J. Electron Spectrosc. **75**, 273 (1995)
66. C.S. Fadley, J. Electron Spectrosc. **178–179**, 2 (2010)
67. K. Kobayashi, M. Kobata, I. Masaaki, H. Iwai, J. Electron Spectrosc. **190**, 210 (2013), and earlier references therein
68. A. Winkelmann, J. Garcia de Abajo, C.S. Fadley, New J. Phys. **10**, 113002 (2008)
69. F.J. Garcia de Abajo, Online photoelectron diffraction program. Available at http://nanophotonics.csic.es/widgets/edac/
70. I. Bartos et al., Phys. Rev. B **83**, 235327 (2011)
71. M. Kobata et al., Surf. Interface Anal. **43**, 1632 (2011)
72. S. Hellman et al., Phys. Rev. B **85**, 075109 (2012)
73. L.-P. Oloff et al., New J. Phys. **16**, 123045 (2014)
74. E.D. Tober et al., J. Electron Spectrosc. **189**, 152 (2013)

75. F. Krasniqi, B. Najjari, L. Struder, D. Rolles, A. Voitkiv, J. Ullrich, Phys. Rev. A **81**, 033411 (2010)
76. X.S. Sun, A.X. Gray, A.P. Kaduwela, C.S. Fadley, Phys. Rev. A **89**, 053415 (2014)
77. C. Wiemann et al., Appl. Phys. Lett. **100**, 223106 (2012)
78. M. Patt et al., Rev. Sci. Inst. **85**, 113704 (2014)
79. F. Kronast, Appl. Phys. Lett. **93**, 243116 (2008)
80. A.X. Gray et al., Appl. Phys. Lett. **97**, 062503 (2010)
81. S.-H. Yang, B.C. Sell, C.S. Fadley, J. Appl. Phys. **103**, 07C519 (2008)
82. S.-H. Yang, B.C. Sell, B.S. Mun, C.S. Fadley, Probing buried layers and interfaces with soft X-ray standing wave spectroscopies, in ed. by J. Zegenhagen, A. Kazimirov, The X-ray Standing Wave Technique: Principles and Applications, Vol. 7 in the Series on Synchrotron Radiation and Applications (World Scientific, Singapore, 2013)
83. S.-H. Yang, A.X. Gray, A.M. Kaiser, B.S. Mun, J.B. Kortright, C.S. Fadley, J. Appl. Phys. **113**, 073513 (2013); A versatile downloadable software package for calculating such effects, the Yang X-ray Optics (YXRO) program, is also available at https://sites.google.com/a/lbl.gov/yxro/home
84. A.X. Gray et al., Phys. Rev. B **82**, 205116 (2010)
85. A.M. Kaiser et al., Phy. Rev. Letters **107**, 116402 (2011)
86. A.X. Gray et al., Europhys. Lett. **104**, 17004 (2013). Reprint with Supplementary Information at http://www.physics.ucdavis.edu/fadleygroup/SWARPES_EPL_104_17004_2013.reprint.pdf
87. S. Döring et al., Phys. Rev. B **83**, 165444 (2011)
88. A.A. Greer et al., Appl. Phys. Lett. **101**, 202402 (2012)
89. C. Papp, G. Conti et al., J. Appl. Phys. **112**, 114501 (2012)
90. B.L. Henke, Phys. Rev. A **6**, 94 (1972)
91. M. Mehta, C.S. Fadley, Phys. Lett. **55A**, 59 (1975)
92. M. Mehta, C.S. Fadley, Chem. Phys. Lett. **46**, 225 (1977)
93. M.J. Chester, T. Jach, S. Thurgate, J. Vac. Sci. Tech. **B11**, 1609 (1993)
94. J. Kawai, S. Hayakawa, Y. Kitajima, Y. Gohshi, Adv. X-ray Chem. Anal. Jpn. 26s, 97–102 (1995)
95. J. Kawai, J. Electron Spectrosc. Relat. Phenom. **178–179**, 268 (2010)
96. M. Marinova, J.E. Rault et al., Nano Lett. **15**, 2533 (2015)
97. H. Yamada et al., Sci. Repts. **3**, 2834 (2013)
98. J.C. Woicik, E.J. Nelson, P. Pianetta, Phys. Rev. Lett. **84**, 773 (2000)
99. J.C. Woicik, E.J. Nelson, T. Kendelewicz et al., Phys. Rev. B **63**, 041403(R) (2001)
100. J.C. Woicik, E.J. Nelson, D. Heskett et al., Phys. Rev. B **64**, 125115 (2001)
101. J.C. Woicik, E.J. Nelson, L. Kronik et al., Phys. Rev. Lett. **89**, 077401 (2002)
102. V. Strocov et al., J. Synchrotron Rad. **21**, 32 (2014) and earlier references therein
103. J. Braun, J. Minar et al., Phys. Rev. B **88**, 205409 (2013)
104. S. Nemšák et al., to be published
105. M. Salmeron, R. Schlögl, Surf. Sci. Rep. **63**, 169 (2008)
106. D.E. Starr, Z. Liu, M. Hävecker, A. Knop-Gericke, H. Bluhm, Chem. Soc. Rev. **42**, 5833 (2013)
107. S. Nemšák, A. Shavorskiy et al., Nature Comm. **5**, 5441 (2014)
108. O. Karslıoğlu, S. Nemšák, et al., Faraday Soc. Disc. 180, 35 (2015). doi:10.1039/C5FD00003C

http://www.springer.com/978-3-319-24041-1

Hard X-ray Photoelectron Spectroscopy (HAXPES)

Woicik, J.C. (Ed.)
2016, XII, 571 p. 279 illus., 180 illus. in color.,
Hardcover
ISBN: 978-3-319-24041-1